J. Fluid Mech. (2014), *vol.* 751, *pp.* 570–600.
doi:10.1017/jfm.2014.314

Low-Reynolds-number wakes of elliptical cylinders: from the circular cylinder to the normal flat plate

Mark C. Thompson[1,†], Alexander Radi[1], Anirudh Rao[1], John Sheridan[1] and Kerry Hourigan[1,2]

[1]Fluids Laboratory for Aeronautical and Industrial Research (FLAIR), Department of Mechanical and Aerospace Engineering, Monash University, Melbourne, Victoria 3800, Australia

[2]Division of Biological Engineering, Monash University, Melbourne, Victoria 3800, Australia

(Received 22 October 2013; revised 20 March 2014; accepted 29 May 2014)

While the wake of a circular cylinder and, to a lesser extent, the normal flat plate have been studied in considerable detail, the wakes of elliptic cylinders have not received similar attention. However, the wakes from the first two bodies have considerably different characteristics, in terms of three-dimensional transition modes, and near- and far-wake structure. This paper focuses on elliptic cylinders, which span these two disparate cases. The Strouhal number and drag coefficient variations with Reynolds number are documented for the two-dimensional shedding regime. There are considerable differences from the standard circular cylinder curve. The different three-dimensional transition modes are also examined using Floquet stability analysis based on computed two-dimensional periodic base flows. As the cylinder aspect ratio (major to minor axis) is decreased, mode A is no longer unstable for aspect ratios below 0.25, as the wake deviates further from the standard Bénard–von Kármán state. For still smaller aspect ratios, another three-dimensional quasi-periodic mode becomes unstable, leading to a different transition scenario. Interestingly, for the 0.25 aspect ratio case, mode A restabilises above a Reynolds number of approximately 125, allowing the wake to return to a two-dimensional state, at least in the near wake. For the flat plate, three-dimensional simulations show that the shift in the Strouhal number from the two-dimensional value is gradual with Reynolds number, unlike the situation for the circular cylinder wake once mode A shedding develops. Dynamic mode decomposition is used to characterise the spatially evolving character of the wake as it undergoes transition from the primary Bénard–von Kármán-like near wake into a two-layered wake, through to a secondary Bénard–von Kármán-like wake further downstream, which in turn develops an even longer wavelength unsteadiness. It is also used to examine the differences in the two- and three-dimensional near-wake state, showing the increasing distortion of the two-dimensional rollers as the Reynolds number is increased.

Key words: absolute/convective instability, vortex streets, wakes

† Email address for correspondence: mark.thompson@monash.edu

1. Introduction

The circular cylinder has formed the basis of a large body of fundamental research on bluff body wakes for over a century starting with the works of Strouhal (1878), Bénard (1908), Kármán (1911) and numerous studies since (e.g. Roshko 1954; Taneda 1959; Norberg 1987; Monkewitz 1988; Williamson 1988; Eisenlohr & Eckelmann 1989; Strykowski & Sreenivasan 1990; Albarede & Monkewitz 1992; Dusek, Le Gal & Fraunie 1994; Zhang *et al.* 1995; Barkley & Henderson 1996; Thompson, Hourigan & Sheridan 1996; Williamson 1996*a*,*b*; Henderson 1997; Thompson, Leweke & Williamson 2001; Kumar & Mittal 2006; Behara & Mittal 2010; Kumar & Mittal 2012, and many, many, others). This can be attributed to a number of factors including its symmetry, relevance to industry applications such as oil rig risers, chimneys, transmission wires, amongst other things and perhaps even the intrinsic aesthetic beauty of the laminar wake. Of interest to the current paper, the near- and far-wake states have been explored and documented, as have the three-dimensional transitions that lead to a turbulent wake as the Reynolds number is increased.

On the other hand, there has been much less research on the wakes of other slightly less symmetrical bodies such as elliptic cylinders, with this body shape mainly investigated for very low (Shintani, Umemura & Takano 1983) or high Reynolds numbers (Modi & Wiland 1970; Modi & Dikshit 1975; Ota, Nishiyama & Taoka 1987), and even then mostly for non-zero angles of attack.

An investigation by Modi & Dikshit (1975) examined the vortex spacing and arrangement in the wake of elliptic cylinders for eccentricities in the range $0.44 \leqslant \epsilon \leqslant 0.98$ for $Re = 68\,000$. It was found that a lower eccentricity leads to rapid changes in the longitudinal and lateral vortex spacing in the wake away from the circular cylinder case. Also focusing on the high-Reynolds-number case, Ota *et al.* (1987) examined the wakes of elliptic cylinders in the range $35\,000 \leqslant Re \leqslant 125\,000$ in terms of the universal Strouhal number introduced by Roshko (1954), based on wake width and shear-layer velocity, showing that this Strouhal number was insensitive to angle of attack.

At lower Reynolds numbers, Jackson (1987) used two-dimensional finite-element simulations and stability analysis to determine the critical Reynolds numbers for the initial steady-to-unsteady transition. This was done for a range of body shapes including elliptic cylinders. The critical Reynolds number of a circular cylinder was determined as 45.4, while for a flat plate it reduces to 27.8. More recent estimates for a circular cylinder determine the value as 47.3 (Kumar & Mittal 2006) using a blockage of just 0.5 %, while Saha (2013) estimated the value for a 7 % deep flat plate as 32.45, although the blockage was much higher at 5 %.

Johnson, Thompson & Hourigan (2004) examined the near-to-far-wake two-dimensional transitions for elliptic cylinders of various aspect ratios for $75 \leqslant Re \leqslant 175$. For certain Reynolds number/aspect ratio ranges, there was a transition from the near-wake shedding frequency to a non-commensurate far-wake frequency. The far wake resembled the standard Bénard–von Kármán (BvK) wake but was formed from an instability of the time-mean near wake, which had transformed into a two-layered structure. The secondary shedding could occur either far downstream after the individual near-wake vortices had diffused and merged so that they were not identifiable, or prior to this, when they were clearly distinguishable. In either case, the ratio of the near- and far-wake frequencies was not a simple ratio, and so the secondary wake was not primarily due to merging of primary vortices. At even smaller aspect ratios and higher Reynolds number, the secondary wake developed a characteristic waviness, and even vortex merging in the secondary wake could

be observed. These observations are broadly in line with the behaviour of circular cylinder wakes investigated by Cimbala, Nagib & Roshko (1988), Williamson & Prasad (1993) and Kumar & Mittal (2012), although for the circular cylinder, the transition occurs at higher Reynolds numbers and far downstream. In any case, the introduction of eccentricity to the otherwise circular cylinder leads to a whole range of wake states not observed in the rotationally symmetric case. More recently, Aleksyuk, Shkadova & Shkadov (2012) examined a small-aspect-ratio elliptic cylinder, again showing the development of the secondary wake within 40 diameters for $Re = 100$.

The normal flat plate can be considered to be an elliptic cylinder with zero aspect ratio. Owing to its simplicity and rotational symmetry, it has been studied more than elliptic cylinders, with perhaps the first extensive study by Fage & Johansen (1927), who determined the vortex spacing in the wake. Even for small Reynolds number of the order of 100, the near wake undergoes a rapid downstream transition to a two-layered wake with two lines of like-signed vortices offset on each side of the centreline. However, less knowledge exists on the nature of this wake in general. Najjar & Balachandar (1998) used three-dimensional simulations to examine the wake state at $Re = 250$. The three-dimensionality was observed to have a spanwise wavelength of 1.2 plate widths, perhaps reminiscent of mode B for a circular cylinder. The three-dimensional transitions were examined by Thompson *et al.* (2006*b*) using Floquet stability analysis. They showed that an initial quasi-periodic transition occurred at Reynolds numbers slightly above $Re = 100$. This mode has a wavelength of approximately five diameters. At slightly higher Reynolds numbers, a second three-dimensional mode became unstable with a much shorter wavelength. That mode was periodic with the two-dimensional base flow. This second mode appears to have been observed in the wake of inclined plates up to $Re = 350$ by Yang *et al.* (2012).

As discussed above for elliptic cylinders, a secondary vortex street develops downstream of the primary vortex street (Taneda 1959; Johnson *et al.* 2004; Saha 2007, 2013), which has been attributed to a hydrodynamic instability of the mean wake. Apart from viscous diffusion, the geometric arrangement of the vortices in the vortex street determines whether it is predominately stable or whether it breaks down into parallel shear flow. A critical value was derived by Durgin & Karlsson (1971) as $h/a = 0.365$, where h is the cross-wake spacing between positive and negative wake vortices and a is the separation between vortices of the same sign. Above this critical value, the vortices stretch out and align with the downstream direction leading to a parallel shear flow. In turn, this mean shear flow can become unstable forming a secondary vortex street. Karasudani & Funakoshi (1994) examined this process further using a point vortex method to examine the evolution of an idealised street for vortex spacings of 0.31 and 0.41. For $h/a = 0.31$, the initial vortices remain isolated, while for $h/a = 0.41$ the vortices rotate to align with their major axis in the streamwise direction and stretch and diffuse until they form a nearly parallel shear flow.

The aim of this study is to examine a variety of aspects of the wakes of elliptic cylinders, including the circular cylinder and the flat plate as the two extreme cases. This includes characterising the initial transition to periodic flow, the near- and far-wake transitions, transition to a three-dimensional wake state, Strouhal number and drag coefficient variations with Reynolds number, the saturated three-dimensional mode states for the flat plate, and using dynamic mode decomposition (DMD) to characterise some of the complex wake states. Most of the analysis is based on two-dimensional simulations and linear or Floquet stability analysis based on these two-dimensional simulations; however, a few full three-dimensional simulations are used to explore special cases. The study proceeds by describing the problem and

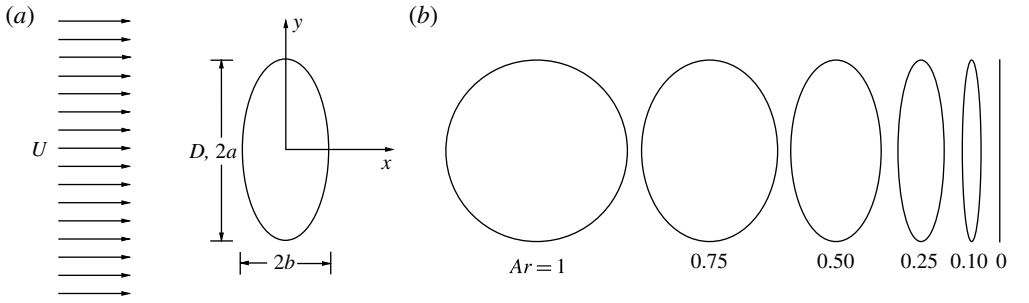

FIGURE 1. (*a*) Problem definition including relevant dimensions. (*b*) The elliptic cylinders considered in this study include the special cases of the circular cylinder with aspect ratio unity and the normal flat plate which corresponds to a zero-aspect-ratio cylinder.

numerical approaches before examining the results of two- and three-dimensional simulations. Some results from a parallel experimental program (Radi *et al.* 2013), which is not the focus of the current paper, are included for direct comparisons. Mostly, the analysis and interpretations are framed in terms of known results for the circular cylinder and, to a lesser extent, the normal flat plate.

2. Numerical approach

2.1. *Problem definition*

The current paper addresses the flow past two-dimensional elliptic cylinders with the major axis placed normal to the flow direction, as shown in figure 1. The aspect ratio is defined by the ratio of the semi-minor (b) to semi-major (a) axis length, i.e. $Ar = b/a$, and for convenience for comparisons with the circular cylinder, it is useful to define $2a = D$, the diameter of the circular cylinder. Thus, $Ar = 0$ corresponds to a flat plate placed normal to the flow and $Ar = 1$ corresponds to a circular cylinder. The Reynolds number is based on the major axis length, i.e. $Re = U(2a)/\nu$, where U is the oncoming uniform flow speed and ν is the kinematic viscosity. This paper concentrates on the two- and three-dimensional wake transitions as the aspect ratio changes. There is a parallel experimental program that used flow visualisation and particle image velocimetry to examine these flows, the results of which will appear elsewhere (Radi *et al.* 2013); however, limited experimental comparisons will be given with the numerical results that form the basis of this paper.

2.2. *Numerical method*

The flow is solved numerically using a two-dimensional spectral-element method, which has been validated in many previous related studies (e.g. Thompson *et al.* 1996, 2006*a*; Thompson, Leweke & Hourigan 2007; Griffith *et al.* 2008, 2010; Stewart *et al.* 2010; Leontini, Lo Jacono & Thompson 2013; Rao *et al.* 2013*a*), and so will only be briefly described here. The computational domain is broken up into a macro-element mesh, with elements that can have curved sides. Each macro-element is internally subdivided into a $n_x \times n_y$ nodes, spaced according the Gauss–Legendre–Lobatto quadrature points and, within each element, the velocity components and pressure are represented by the tensor product of Lagrangrian interpolating polynomials. Importantly, the method has been shown to possess spectral spatial convergence

as the polynomial order is increased. In the current implementation, a three-step fractional-step method (e.g. Chorin 1968; Karniadakis & Sherwin 2005) is used for the temporal discretisation, which is formally second-order accurate.

A few simulations were performed using a three-dimensional spectral/spectral-element code to investigate the three-dimensional saturated flow states for the normal flat plate. This parallel code is based on the two-dimensional spectral-element code, but uses a Galerkin Fourier expansion in the spanwise direction (e.g. see Karniadakis & Triantafyllou 1992; Thompson *et al.* 1996).

The boundary conditions were specified as uniform flow $(U, 0)$ at the inflow and side boundaries, which were positioned 50 major axis lengths from the cylinder, and constant pressure and zero normal velocity gradient at the outflow boundary. The cylinder surface was a no-slip boundary. At all boundaries except for outflow, a first-order normal pressure gradient condition was used as specified in Karniadakis, Israeli & Orszag (1991). This enforces mass conservation at these boundaries and leads to overall second-order accurate velocity fields.

2.3. *Stability analysis*

Linear and Floquet stability analysis is used to determine the critical transitions as the Reynolds number is increased. This employs the Arnoldi method based on a Krylov subspace of evolved fields, as described by Mamun & Tuckerman (1995) and Barkley & Henderson (1996), and has been utilised for a number of similar problems where more details can be found (Ryan, Thompson & Hourigan 2005; Leontini, Thompson & Hourigan 2007; Chaurasia & Thompson 2012; Rao *et al.* 2013*b*).

2.4. *DMD*

DMD is also used as part of the analysis. This employs a time sequence of fields, in this case velocity fields, to construct a spectral decomposition. This process gives a set of approximations to the Koopman modes, called Ritz vectors, with associated eigenvalues, called Ritz values. The Ritz vectors are a set of complex spatial modes which vary sinusoidally in time at frequencies specified by the argument of the complex eigenvalues. The modes may also grow or decay exponentially in time, according to the magnitude of the associated eigenvalue. The analysis is particularly useful to study behaviour controlled by multiple time scales or frequencies, in order to decouple the spatial behaviour of the different frequency components. Another important point, unlike a standard discrete Fourier transform taken at a point, is that it can extract accurate oscillation frequencies even with a relatively short sequence of fields on which to base the analysis. The approach used here follows closely that fully detailed in Rowley *et al.* (2009) and Schmid (2011), so only a very brief outline is given here.

If $\boldsymbol{x}_0, \boldsymbol{x}_1, \ldots, \boldsymbol{x}_m$ represent a sequence of column vectors (e.g. the velocity fields) corresponding to times $t_0, t_0 + \Delta t, \ldots, t_0 + (m-1)\Delta t$, then it is clear that subsequent fields can be related to previous fields through the matrix equation

$$\begin{bmatrix} \boldsymbol{x}_1 & \boldsymbol{x}_2 & \cdots & \boldsymbol{x}_m \end{bmatrix} = \begin{bmatrix} \boldsymbol{x}_0 & \boldsymbol{x}_1 & \cdots & \boldsymbol{x}_{m-1} \end{bmatrix} \begin{bmatrix} 0 & 0 & \cdots & 0 & \alpha_1 \\ 1 & 0 & \cdots & 0 & \alpha_2 \\ 0 & 1 & \cdots & 0 & \alpha_3 \\ \vdots & & \ddots & & \vdots \\ 0 & 0 & \cdots & 1 & \alpha_m \end{bmatrix} (\equiv \boldsymbol{KC}). \tag{2.1}$$

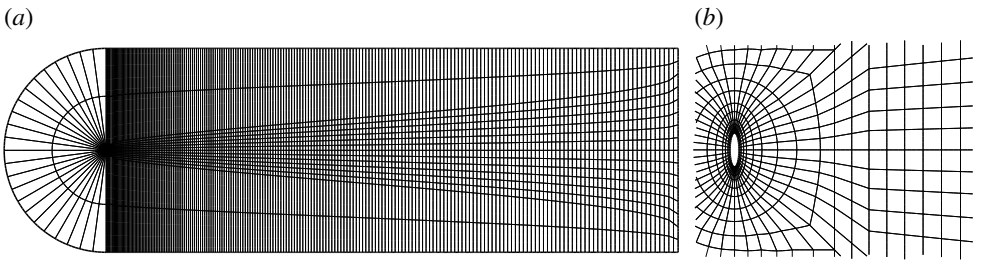

FIGURE 2. (*a*) Mesh used for the $Ar = 0.25$ cylinder. The other meshes are similarly configured. The inflow length is $50D$ and the outflow length $280D$. (*b*) Shows a zoomed in view of the mesh in the neighbourhood of the cylinder. Only macro-elements are shown, which are further subdivided internally.

The right-hand side matrix is called the companion matrix, $\boldsymbol{C}$, and, since all of the columns vectors $\boldsymbol{x}_0, \ldots, \boldsymbol{x}_m$ are known, the unknown terms $\alpha_1, \alpha_2, \ldots$ can be determined by solving an over-determined matrix equation using singular-value decomposition (SVD) or QR decomposition. Then the m eigenvalues (λ_k) and eigenvectors (z_k) of $\boldsymbol{C}$ can be used for a modal reconstruction of the original data set in the form

$$\begin{bmatrix} \boldsymbol{x}_0 & \boldsymbol{x}_1 & \cdots & \boldsymbol{x}_{m-1} \end{bmatrix} = \begin{bmatrix} \boldsymbol{v}_1 & \boldsymbol{v}_2 & \cdots & \boldsymbol{v}_m \end{bmatrix} \begin{bmatrix} 1 & \lambda_1 & \lambda_1^2 & \cdots & \lambda_1^{m-1} \\ 1 & \lambda_2 & \lambda_2^2 & \cdots & \lambda_2^{m-1} \\ \vdots & & \vdots & \ddots & \\ 1 & \lambda_m & \lambda_m^2 & \cdots & \lambda_m^{m-1} \end{bmatrix} (\equiv \boldsymbol{VT}). \quad (2.2)$$

Here, the column vectors $\boldsymbol{v}_k$, called Ritz vectors, are just the column vectors of $\boldsymbol{V} = \boldsymbol{KZ}$, with $\boldsymbol{Z}$ the matrix formed from the column vectors $\boldsymbol{z}_0, \ldots, \boldsymbol{z}_{m-1}$. Note that both the Ritz vectors and values consist of complex conjugate pairs. Equation (2.2) just states that the field at any discrete time t_k can be expressed as a modal expansion

$$\boldsymbol{x}_k = \sum_{i=1}^{m} \lambda_i^k \boldsymbol{v}_i. \quad (2.3)$$

If the sequence of fields is strictly periodic, so that $\boldsymbol{x}_m = \boldsymbol{x}_0$, then the expansion given in (2.3) is equivalent to a Fourier decomposition.

2.5. *Mesh and domain considerations*

A typical mesh is shown in figure 2 for an $Ar = 0.25$ aspect ratio cylinder. The computational domain extends between $-50 \leqslant x/D \leqslant 280$ in the streamwise direction and $-50 \leqslant y/d \leqslant 50$ in the cross-stream direction. This means blockage is restricted to 1 %. The long outflow length allows various two-dimensional wake transitions to occur for the smaller-aspect-ratio bodies. Note that resolution is maintained towards the outflow boundary to resolve the wake fully over the entire domain. For the production runs, each internal element is subdivided into 6×6 node points; increasing the internal resolution to 8×8 resulted in a change in the near-wake Strouhal numbers and the Floquet multipliers for the $Re = 200$ cases of less than 0.01 and 1 %, respectively. Six different aspect ratios were considered: $Ar = 0.0$, 0.10, 0.25, 0.50, 0.75 and 1.0. The Reynolds number range was restricted to $Re \leqslant 200$.

Ar	Re_c	St_c
(Flat plate) 0.00	31.6	0.0998
0.10	33.5	0.1030
0.25	35.6	0.1074
0.50	38.8	0.1120
0.75	42.6	0.1144
(Circular cylinder) 1.00	47.2	0.1163

TABLE 1. Critical Reynolds numbers and Strouhal numbers for the initial steady-to-unsteady-wake transition for elliptic cylinders of different aspect ratios.

3. Results

3.1. *Transition to unsteady flow*

As for the circular cylinder, elliptic cylinders also undergo an initial Hopf bifurcation from a steady to periodic wake flow. This takes place at Reynolds numbers lower than for the circular cylinder, as was shown by Jackson (1987). Table 1 shows the transition Reynolds numbers for the different aspect ratio elliptic cylinders considered. These were from simulations at subcritical Reynolds numbers starting from saved solutions at slightly supercritical Reynolds numbers. The flow was evolved until the oscillation amplitude was decaying purely exponentially, allowing the decay rates to be accurately determined. The critical values could then be determined very accurately by extrapolation to zero growth rate.

For a flat plate, Saha (2007) finds a value of $Re_c = 32.5$, while the early numerical study of Jackson (1987), with a 10 % blockage, found values of $Re_c = 27.8$ and $St_c = 0.124$. The Hopf bifurcation for a circular cylinder has been examined by a number of authors: $Re_c = 45.4$ (Jackson 1987), 46.1 (Dusek *et al.* 1994), 46.7 (Le Gal, Nadim & Thompson 2001), 47.3 (Kumar & Mittal 2006), 49 (Williamson 1996*b*, experimental). For the numerical studies, the differences are mainly due to the different blockage ratios of the grid systems used. The result from Kumar & Mittal (2006) employed the lowest blockage ratio (0.5 %), and hence is the most accurate. (The blockage ratio for the current study is 1 %.) In addition, Kumar & Mittal (2006) gives the critical Strouhal number for the circular cylinder transition to be 0.1163, which was the value found in the current study to four significant figures. Hence, the results given in table 1 are in excellent agreement with previous studies.

3.2. *Two-dimensional shedding*

Aspects of the two-dimensional wake transitions have been considered by a number of authors, both experimentally and numerically: Cimbala (1984), Cimbala *et al.* (1988), Williamson & Prasad (1993), Johnson *et al.* (2004) and Saha (2013), although mainly for a circular cylinder. Johnson *et al.* (2004) examined the transitions using Fourier analysis of time sequences at points along the centreline. That work is extended in this paper. Figures 3 and 4 show the asymptotic wake behaviour in terms of wake vorticity patterns as the aspect ratio and the Reynolds number are varied. For the circular cylinder at $Re = 100$, the near wake is the standard aligned BvK street, which further downstream develops into a two-layered wake, with clockwise vortices forming a line offset from the anticlockwise vortices below. Yet further downstream, the clockwise and anticlockwise vortices diffuse and cross-annihilate, leaving a

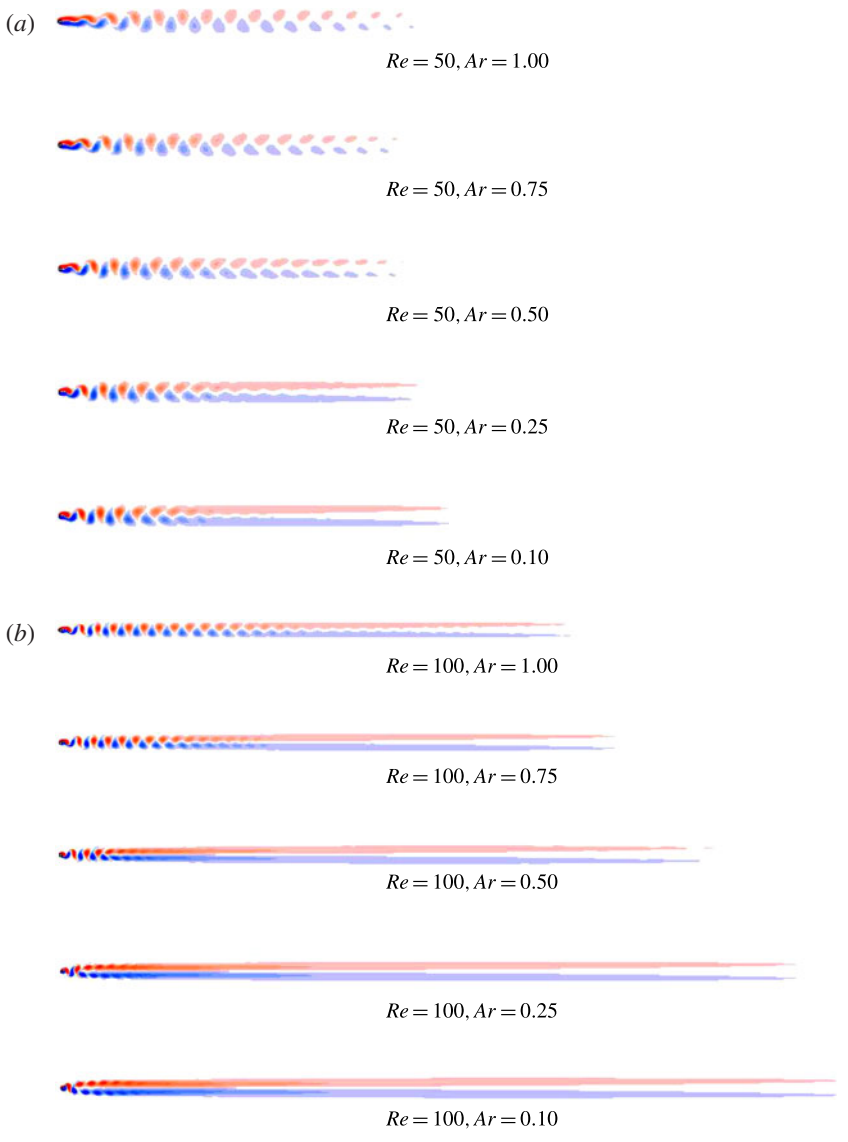

FIGURE 3. (Colour online) Asymptotic wake states for different aspect ratios as the Reynolds number is varied using the vorticity field to highlight the structure: (*a*) $Re = 50$; (*b*) $Re = 100$. The aspect ratios are displayed on the plots. The first 250 diameters of the wake are shown. The flow is from left to right. Blue (darker grey) and red (lighter grey) denote positive and negative vorticity, respectively.

mean wake structure without identifiable individual vortices. Increasing the Reynolds number further to $Re = 200$ means that this evolved mean wake persists much further downstream due to the reduced viscous damping. There is no sign of a secondary wake, despite its appearance in other numerical studies (Kumar & Mittal 2012); the higher accuracy of the spectral-element method presumably leads to less numerical noise to trigger the convective instability. The two-layer wake that develops from the near wake has a reduced streamwise wavelength. For the next smaller aspect ratio

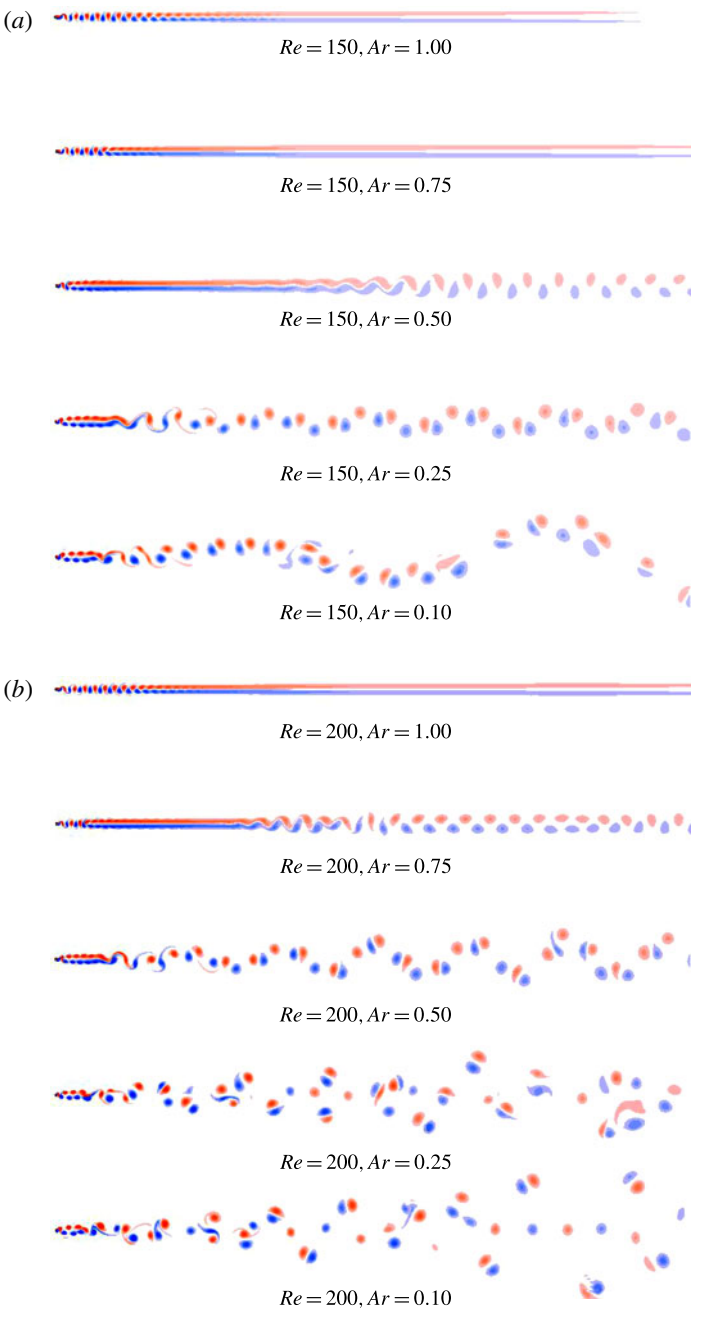

FIGURE 4. (Colour online) As for figure 3 with (*a*) $Re = 150$ and (*b*) $Re = 200$.

cylinder ($Ar = 0.75$), the same sequence of transitions occur but for lower Reynolds numbers, or equivalently closer to the cylinder for the same Reynolds number. This is presumably due to the increased strength of the shed vortices, which will be quantified later. For smaller aspect ratios, the transition process is further accelerated. For instance, for $Ar = 0.5$ at $Re = 200$, the transition from the BvK street to the

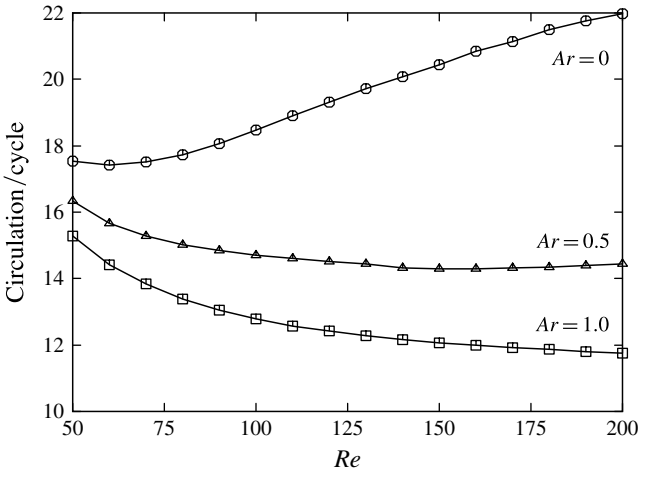

FIGURE 5. Integrated vorticity (i.e. circulation) passing though the top shear layer into the wake from vorticity generated at the front of the cylinder as a function of Reynolds number. The aspect ratios are marked.

two-layered street occurs within the first two diameters of the cylinder, and the stationary wake profile does not form at all. Instead, the identifiable vortices in the two-layer wake interact at approximately $20D$ downstream to form a much longer wavelength secondary vortex street, which itself oscillates spatially with an even longer wavelength. As the aspect ratio is reduced still further, the far wake becomes increasingly complex and chaotic. For $Ar = 0.1$ and $Re = 200$, vortex pairs form as part of the far wake and self-propel away from the centreline. The normal flat plate wakes, not shown, are similar to the $Ar = 0.1$ wakes.

Part of the reason for the different behaviour can be attributed to the increasing vorticity flux feeding into the wake for the smaller-aspect-ratio cases, as the flow has a higher speed as it passes over the top of the cylinder. This is quantified in figure 5, which gives the circulation entering the wake each shedding cycle as the flow separates near the top of the cylinder, and feeds the vorticity generated at the front of the cylinder into the wake. This circulation is given by

$$\Gamma = \int_{one\ period} \left(\int_{1/2}^{\infty} u\omega \, \mathrm{d}y \right) \mathrm{d}t. \tag{3.1}$$

(Note that non-dimensional variables are used.) Clearly, the circulation convecting into the wake is considerably higher for the flat plate compared with that for a circular cylinder. At $Re = 200$, the difference is almost a factor of two. The correspondingly larger circulation per wake vortex has a significant effect on both the near- and far-wake dynamics as is demonstrated in figures 3 and 4.

3.3. *Temporal evolution of the wake for small aspect ratio*

Figure 6 shows the development of the wake through the transient stage for the $Ar = 0.25$ cylinder at $Re = 150$. The initial evolution is similar to that for a circular cylinder, i.e. the development of a long recirculation zone at the rear of the cylinder which becomes unstable and starts to shed vortices. The initial wake then resembles the

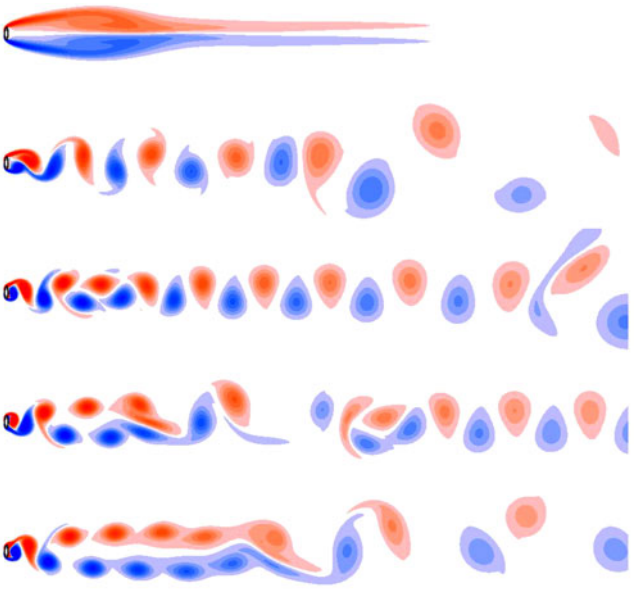

FIGURE 6. (Colour online) Transient development of the wake for $Ar = 0.25$ at $Re = 150$. The images correspond to non-dimensional times: $\tau \equiv tU/D = 100$, 150, 175, 200 and 375. The images are truncated at $x/D = 50$.

standard aligned BvK vortex street. However, after this stage the development deviates. A few diameters downstream of the cylinder, the vortices begin to bunch up, showing the beginnings of a two-layered wake. This is shown in the third image of figure 6, corresponding to a non-dimensional time of 150 units or approximately 50 units after the attached recirculation bubble begins to develop asymmetries. After another 25 time units, the two-layered wake structure is clearly apparent with the secondary wake further downstream formed from merging of those individual two-layer vortices. After a much longer time, the downstream extent of the two-layered wake has increased and the secondary wake structure has become more regular.

3.4. *Transition to a parallel shear flow*

The work of Durgin & Karlsson (1971), Tsuboi & Oshima (1985) and Karasudani & Funakoshi (1994) investigated the stability of the geometrical arrangement of vortices in a wake showing that when the spacing ratio h/a was greater than 0.365, the vortices would rotate to align with the streamwise direction, and stretch out and diffuse resulting in a near-parallel shear flow. If it forms, this near-stationary wake would be convectively unstable and could form a new secondary vortex street with a longer wavelength and lower Strouhal number. Figure 7 plots the variation of the spacing ratio with downstream distance for a number of different aspect ratio elliptic cylinders and Reynolds numbers. Each of these wakes exceed the theoretical transition criterion at some point downstream. The smaller-aspect-ratio ellipses exceed it earlier and by a larger margin. This is consistent with the observed wakes in figures 3 and 4. The images on the right of figure 7 show that the first 50 diameters of the wakes for the cases examined, with the position where the spacing ratio is equal to 0.365 marked with dashed lines. Clearly the stability criterion appears broadly correct,

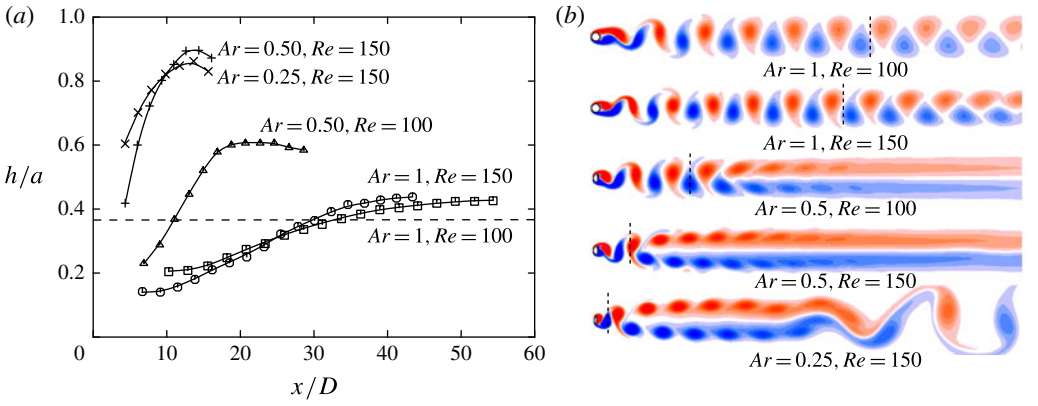

FIGURE 7. (Colour online) (*a*) Downstream variation of the vortex spacing ratio (h/a) for different elliptic cylinders and Reynolds numbers. The dashed line corresponds to a vortex spacing ratio of $h/a = 0.365$. (*b*) The corresponding wakes. The vertical dashed lines show the approximate positions where $h/a = 0.365$.

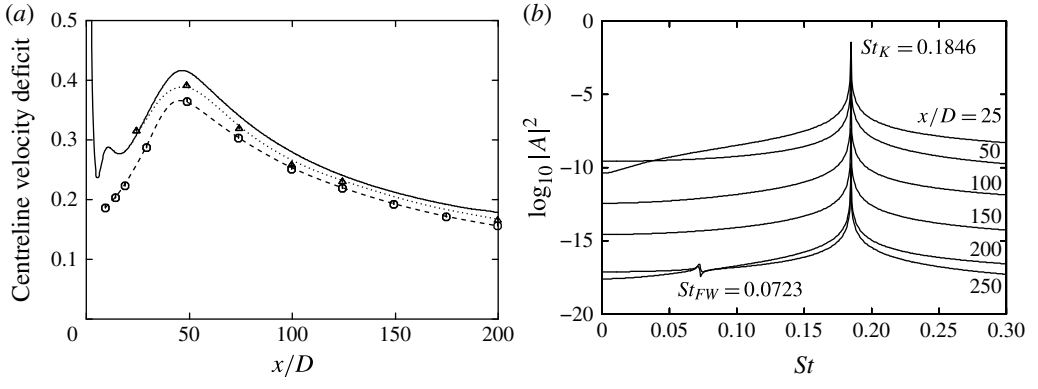

FIGURE 8. (*a*) Comparison of wake deficit ($1 - \overline{u}/U_\infty$) for the circular cylinder at $Re = 150$ with previous experimental results: ○, Williamson & Prasad (1993); △, Cimbala *et al.* (1988). (*b*) Power spectra at various downstream positions showing that the BvK spectral peak is still dominant, although small, even at $x/D = 250$.

although it may be some distance downstream before the parallel shear flow develops. For the $Ar = 0.25$, $Re = 150$ case, the secondary wake develops well before this happens, with the secondary vortices forming from direct merging of a non-integer number of identifiable primary vortices.

3.5. *Variation of mean centreline wake velocity*

For a circular cylinder, the variation of the centreline velocity with downstream distance has been determined experimentally by Cimbala (1984), Cimbala *et al.* (1988) and Williamson & Prasad (1993). In the two-dimensional shedding regime at $Re = 150$, the velocity deficit measured by these authors is shown in figure 8(*a*), together with predictions from the current simulations. In general, the numerical predictions of this deficit are approximately 10 % higher than the results of Williamson & Prasad (1993)

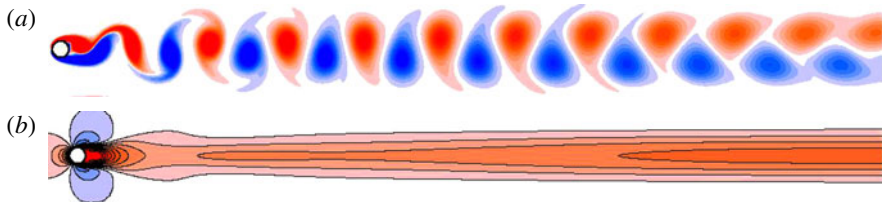

FIGURE 9. (Colour online) (*a*) The development of the vortex street over the first 50 diameters downstream. (*b*) Corresponding coloured (greyscale in print) contours of horizontal velocity component. Here, $Re = 150$, $Ar = 1.0$.

and approximately 5 % above those of Cimbala (1984), but with the overall shape of the distribution predicted very well. Notably, the results from Williamson & Prasad (1993) do not show the small bump in the distribution approximately $10D$ downstream. This small bump seems to corresponds to the transition of a spaced-out BvK vortex street to a more bunched-up street with more diffused vortices, which occurs at approximately $x/D = 10$, as shown in figure 9(*a*). Matching contours of period-averaged horizontal velocity component are shown in figure 9(*b*), showing the effect is relatively subtle on this view. Both images show the wake to $50D$ downstream. The transition to a two-layered wake structure further downstream at approximately $x/D = 45$ corresponds to the main peak in the velocity deficit shown in figure 8(*a*).

From figure 3, it is clear that even at $Re = 200$ (slightly above the Reynolds number of three-dimensional transition), the secondary wake sets in a long way downstream ($x/D > 200$) for the circular cylinder. In fact, for the current simulations, there is no sign of this development in the vorticity plots. However, power spectra at different distances downstream show that the secondary shedding frequency begins to become detectable at $x/D \simeq 200$, and even then the far-wake spectral peak at $St = 0.0723$ is still more than two orders of magnitude below the BvK peak at $x/D = 250$ (figure 8*b*). As indicated above, Kumar & Mittal (2012) examined this case through numerical simulations recently. They found the far-wake spectral peak began to dominate the BvK peak for $x/D \gtrsim 150$. They also found that reducing the time step also reduced the numerical error, which in turn reduced the far-wake spectral peak and increased the downstream position for effective onset. On the other hand, upstream noise in experiments generally causes onset even earlier. For instance, Vorobieff, Georgiev & Ingber (2002) using a flowing soap film, found the onset of the secondary wake to occur at $x/D \simeq 80$. The centreline velocity profiles for other aspect ratios are shown in figure 10. These show substantially different behaviour as the Reynolds number is varied, in line with the image sets shown in figures 3 and 4. A decrease in aspect ratio is clearly associated with an increase in the wake deficit on the centreline. For example, for $Ar = 0.5$ at $Re = 150$, there is a region where the centreline velocity is less than 10 % of the free stream for $5 \lesssim x/D \lesssim 20$, corresponding to where the wake has a two-layered structure. This is apart from the near-wake mean recirculation zone at the start of the wake. As the body is deformed towards a flat plate, this effect is amplified, as recently shown by Saha (2013). For an elliptical cylinder with $Ar = 0.25$, the centreline mean wake velocity is almost zero between $3 \lesssim x/D \lesssim 20$ for $Re = 150$. This case is interesting, as it will be shown later, in that the wake is still two-dimensional at this and higher Reynolds numbers for this aspect ratio.

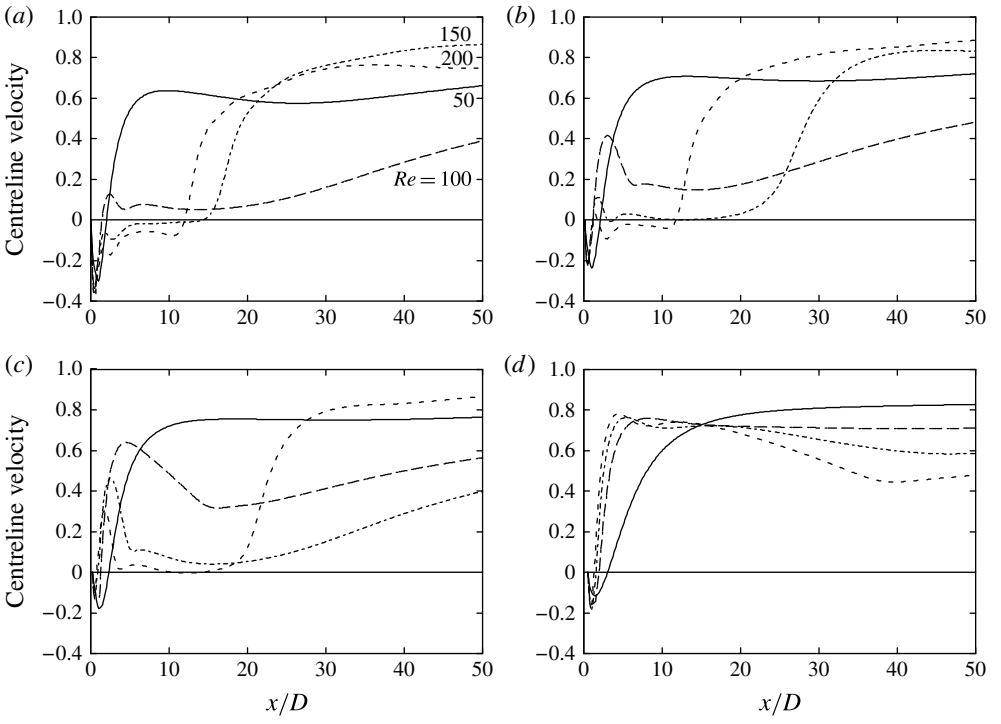

FIGURE 10. Mean velocity on the centreline as the Reynolds number is varied ($Re = 50$, 100, 150, 200): (*a*) $Ar = 0.0$; (*b*) $Ar = 0.25$; (*c*) $Ar = 0.50$; (*d*) $Ar = 1.0$. Solid line, $Re = 50$; long dash, $Re = 100$; short dash, $Re = 150$; medium dash, $Re = 200$.

3.6. *Strouhal–Reynolds number variation*

The Strouhal–Reynolds number variation for a circular cylinder has been documented by a number of authors, e.g. Roshko (1954), Barkley & Henderson (1996) and Williamson (1996*a*), with Williamson (1996*b*) citing a more complete list. Figure 11 shows the *St–Re* variations obtained from two-dimensional simulations for the set of elliptical cylinders studied. The curve for $Ar = 0.75$ is only slightly shifted from the circular cylinder curve. The lower-aspect-ratio curves show distinctly different behaviour, reaching a maximum Strouhal number at increasingly smaller Reynolds numbers as the aspect ratio is reduced. For low Reynolds numbers ($Re \leqslant 60$), the curves appear to approach an envelope curve as the aspect ratio is reduced.

Figure 12 shows a comparison of the numerically predicted Strouhal/Reynolds number variations against those obtained from experiments (Radi *et al.* 2013). The four aspect ratio pairs shown do not match perfectly, nevertheless they are relatively close. (The cylinders used in the experiments were designed to have the same aspect ratios; however, the measured values of the manufactured cylinders were slightly different.) Also note that the $Ar_e = 0.07$ aspect ratio cylinder is actually a sharp-edged rectangular cylinder with an aspect ratio of 7 %.

There are a number of things to note about these comparisons. For the circular cylinder, the numerical and experimental curves match to better than 1 % up to $Re \simeq 177$, at which point the experimental flow becomes three-dimensional as the flow undergoes mode A transition. During this hysteretic transition, the Strouhal number drops considerably, consistent with other experiments (e.g. Williamson 1996*a*).

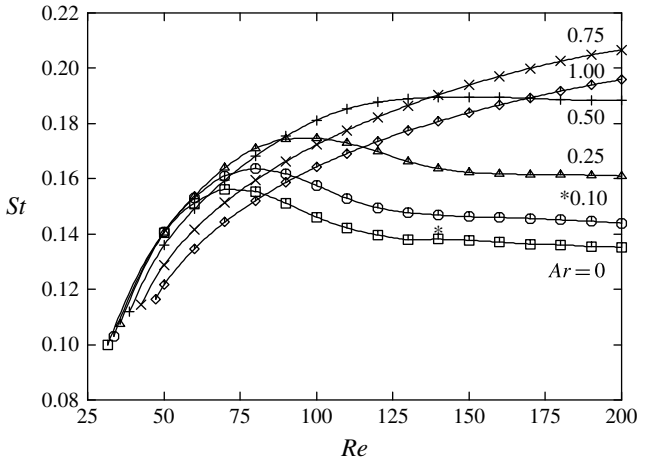

FIGURE 11. Strouhal number variation with Reynolds number from two-dimensional simulations. Each curve corresponds to a different aspect ratio as marked. The asterisks correspond to approximate Strouhal numbers for the flat plate ($Ar = 0$) obtained from direct three-dimensional simulations.

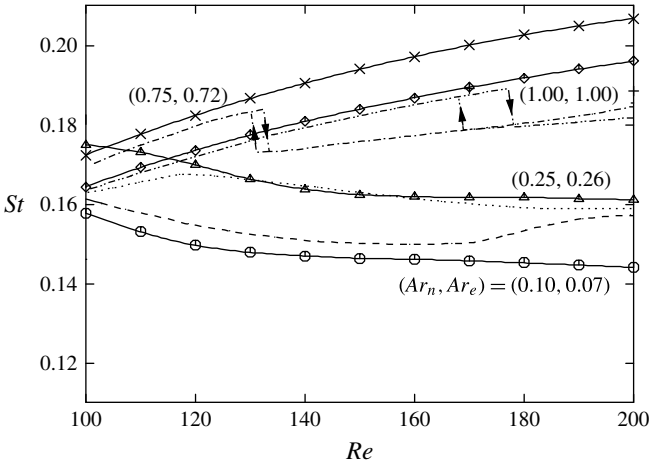

FIGURE 12. Comparison of numerical (solid) and experimental (dashed) Strouhal/Reynolds number variations. Here, (Ar_n, Ar_e) indicates (pairs of similar) numerical and experimental aspect ratios.

On decreasing Reynolds number, the transition from three-dimensional flow back to two-dimensional flow occurs at $Re \simeq 169$. For the next-lowest aspect ratio pair, (Ar_n, Ar_e) = (0.75, 0.72), the three-dimensional transition occurs at a considerably lower Reynolds number, and the hysteric range is much smaller: $130 \leqslant Re \leqslant 132$. As for the circular cylinder, the experimental and numerical Strouhal number curves are still very close in the two-dimensional shedding regime. For the third aspect ratio pair, (Ar_n, Ar_e) = (0.25, 0.26), perhaps surprisingly, the curves match better at the higher Reynolds number range $120 \leqslant Re \leqslant 200$, and deviate at lower Reynolds numbers. The final aspect ratio pair, (Ar_n, Ar_e) = (0.10, 0.07), shows good agreement between the

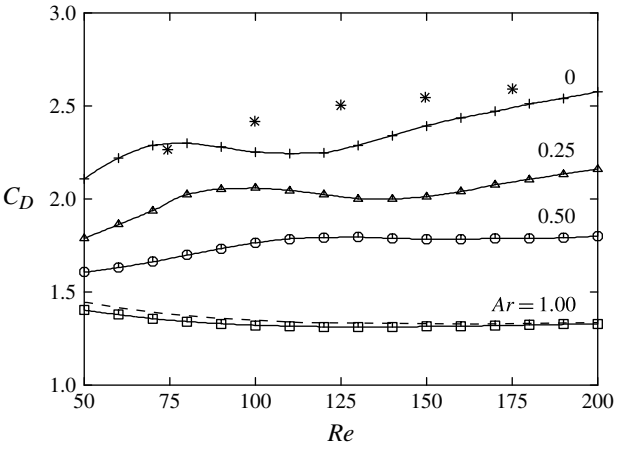

FIGURE 13. Drag coefficient variation with Reynolds number from two-dimensional simulations. The aspect ratio is marked. The dashed line corresponds to the numerical results from Henderson (1995) for the circular cylinder. The discrepancy is probably due to slightly higher blockage of the Henderson (1995) results, although the blockage was not stated in that paper. The asterisks correspond to a 7 % width flat plate with 5 % blockage (Saha 2013). The current blockage ratio is 1 %.

predictions and the measurements for $100 \leqslant Re \leqslant 170$, beyond which the two curves begin to move apart.

3.7. *Drag–Reynolds number variation*

The variation of drag coefficient with Reynolds number is given in figure 13 for aspect ratios: 0, 0.25, 0.5 and 1. The benchmark results of Henderson (1995) are overlaid for the circular cylinder, showing a match up of better than 2 % over most of the range. The discrepancy is most likely due to a slightly higher blockage ratio for the previous results, although the blockage is not given in Henderson (1995). In addition, some results from Saha (2013) are provided for the flat plate. For those, the blockage was 5 %, and the flat plate had 7 % thickness, so it is not surprising there is a greater difference in the predictions for this geometry. The lower-aspect-ratio cases show higher drag and also more complex variation with Reynolds number.

3.8. *Three-dimensional transition*

Similar to the study of Barkley & Henderson (1996), Floquet analysis was used to determine the initial three-dimensional transitions. The critical Reynolds numbers for (the equivalent of) the mode A transition is given in table 2.

The critical Reynolds number decreases significantly with aspect ratio, dropping from $Re_{c,A} = 190.3$ to 88.2 as the aspect ratio is reduced from $Ar = 1$ to 0.25. The critical Reynolds numbers from experiments are somewhat lower than the numerical results: $Re_{c,A} = 177$ against 190.3 for $Ar = 1.0$, and 132 against 148.6 for $Ar = 0.72$ (0.75). Barkley & Henderson (1996) found $Re_{c,A} = 188.5 \pm 1$ also using Floquet analysis, which is close to the value found here, again with the difference likely to be due to slightly different blockage ratios. The lower critical Reynolds numbers from the experiments are consistent with other results for a circular cylinder, where

Ar	Numerical		Experimental	
	$Re_{c,A}$	$\lambda_{c,A}$	$Re_{c,A}$	$\lambda_{c,A}$
(Flat plate) 0.00	—	—		
0.10	—	—		
0.25	88.2	5.34		
0.50	112.2	4.38		
0.75	148.6	3.92	132	∼4
(Circle) 1.00	190.3	3.98	177	∼4

TABLE 2. Critical Reynolds numbers and corresponding wavelengths for mode A transition.

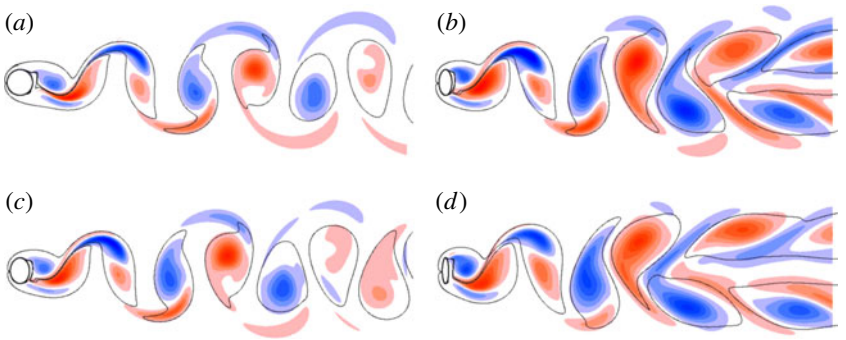

FIGURE 14. (Colour online) Comparison of the mode A streamwise vorticity structure as the ellipse eccentricity is varied showing that the near-wake perturbation field structure is essentially the same: (*a*) $Ar = 1.0$, $Re = 190$, $\lambda/D = 4$; (*d*) $Ar = 0.75$, $Re = 150$, $\lambda/D = 4.0$; (*a*) $Ar = 0.50$; $Re = 110$, $\lambda/D = 4.4$; and (*d*) $Ar = 0.25$; $Re = 90$, $\lambda/D = 5.2$.

background perturbations and end effects can lead to similar early transition (e.g. Williamson 1988, 1989), although Miller & Williamson (1994) found the transition could be delayed beyond $Re_{c,A} = 200$ using contaminating end conditions.

The preferred wavelength at transition $\lambda_{c,A}$ only varies weakly over this aspect ratio range, increasing, although not quite monotonically, from 3.98 to 5.34. Interestingly, mode A remains subcritical for the two smallest aspect ratios. For $Ar = 0.1$, the Floquet multiplier attains a value of $\mu \simeq 1$ at $(Re, \lambda) = (85, 6.0)$, indicating neutral stability, but decreases at higher Reynolds numbers. Hence, if it is unstable at all, it is only marginally unstable and, if so, for only a narrow range of Reynolds numbers before it restabilises.

Evidence that the initial transition is effectively equivalent to the same instability mode as mode A, previously identified for a circular cylinder wake, is shown in figure 14. This shows the streamwise perturbation vorticity field near onset for aspect ratios $Ar = 1.0$, 0.75, 0.50 and 0.25. Clearly, in the near-wake the mode structure is retained, as the aspect ratio (and Reynolds number) varies considerably. For the smaller-aspect-ratio cases, the wake, shown by the thin black lines, undergoes a rapid transition to a two-layered wake structure, as can be seen towards the downstream end of the images. For still smaller aspect ratios ($Ar = 0.1$ or 0), the wake does not experience the mode A transition, possibly because the two-layered wake moves even further upstream, which presumably modifies the near wake sufficiently so that

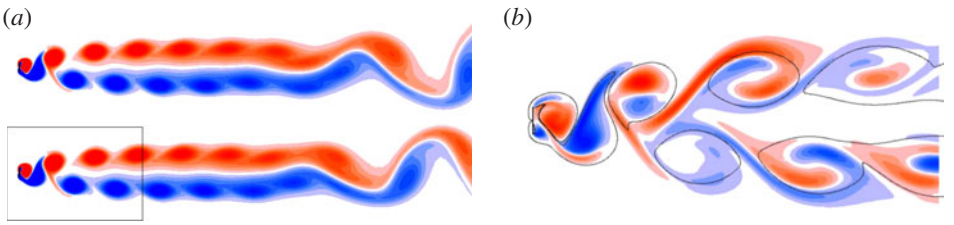

FIGURE 15. (Colour online) (*a*) Snapshots of the spanwise vorticity field of the flat plate wake at $Re = 120$ at one (near-wake) period apart. The downstream transition to secondary shedding prevents the wake being exactly periodic. Nevertheless, over the near-wake region marked by the box, the flow is very close to periodic. The Floquet analysis was performed by evolving the flow in addition to the perturbation fields and restricting the calculation of Floquet multipliers to the boxed region only. (*b*) Streamwise perturbation vorticity for the initial transition mode for the flow past a flat plate at $Re = 120$, close to the transition Reynolds number. Even the near-wake structure is very far from the standard BvK wake of a circular cylinder and there is little resemblance to the mode A wake structure. The mode appears to be reasonably close to subharmonic, with a Floquet multiplier of $1.08e^{0.78\pi i}$.

mode A can no longer reach positive growth. These results were obtained using an outflow domain length of $20D$, which was short enough to ensure that the wake was purely periodic, allowing standard Floquet stability analysis to be performed. Increasing the outflow length, especially for the lower-aspect-ratio cases, allows the wake to undergo secondary transition further downstream with a different frequency than the near-wake shedding frequency. This is discussed in detail later in the paper.

For the zero-thickness flat plate, the initial transition is to a complex Floquet mode, meaning that the frequency of the mode is different from the wake frequency. This mode was previously identified in Thompson *et al.* (2006*b*). It becomes unstable at $Re_c \simeq 116$ for a spanwise wavelength of $\lambda_c \simeq 5.0D$. The critical Reynolds number given here is slightly higher than that suggested in Thompson *et al.* (2006*b*) of $Re_c = 105$–110. In that study, a short outflow length was used to enforce exact wake periodicity, by preventing the transition to secondary shedding further downstream. That seems to have had the effect of reducing the critical Reynolds number slightly. For the case here, a longer domain is used, with an outflow length of $50D$. This causes the wake velocity signal to no longer be strictly periodic even in the near wake. Given this, Floquet stability analysis cannot be strictly applied; however, it can be applied in an approximate sense by determining the growth multipliers over the average period. Taking the $Re = 120$ case as an example, the measured period at $x = 1.5D$ downstream on the centreline varies by approximately 0.3 % between approximately 7.17 and 7.19 over different periods. This is due to the downstream transition to a secondary shedding mode having an upstream effect on the near wake. As well as using the average near-wake period, it is also necessary to restrict the analysis by only taking account of the fields in the near wake, and not including the downstream wake where secondary transition has already occurred, to compute the (pseudo-)Floquet multipliers (see figure 15*a*). This procedure resulted in the computation of Floquet multipliers that typically varied by less than 0.1 % from cycle to cycle. The streamwise perturbation vorticity field for this mode is shown in figure 15(*b*), demonstrating that the perturbation field structure is quite different to mode A.

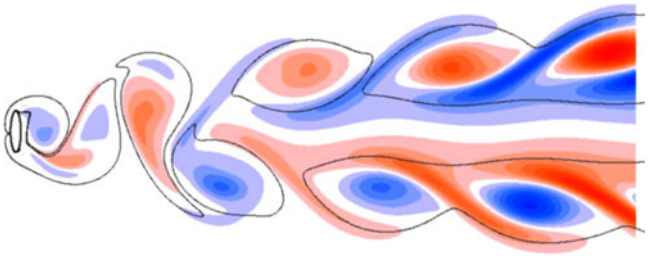

FIGURE 16. (Colour online) Streamwise perturbation vorticity field corresponding to mode A for $Re = 120$ and $\lambda = 4.6D$.

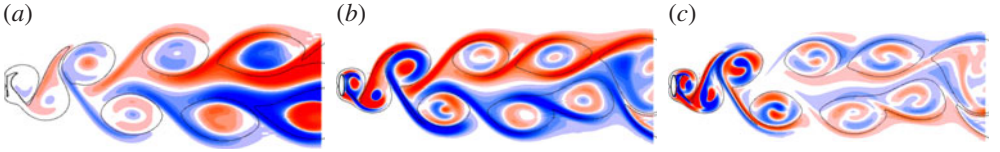

FIGURE 17. (Colour online) Streamwise perturbation vorticity field corresponding to mode AA for $Re = 140$ for the $Ar = 0.00$ cylinder (a) and $Re = 190$ for $Ar = 0.25$ (b). The right-hand image (c) shows the corresponding spanwise perturbation vorticity field for the $Ar = 0.25$ cylinder at $Re = 190$.

3.9. *Three-dimensionality past transition*

Decreasing the aspect ratio results in progressively more rapid downstream transition to the two-layered vortex street. For the $Ar = 0.25$ aspect ratio cylinder, mode A initially becomes unstable at $Re = 88$; however, the mode is no longer unstable beyond $Re \simeq 120$–125. Figure 16 shows the streamwise perturbation vorticity field at $Re = 120$ for $\lambda = 4.6D$. At this point it is still unstable with a Floquet multiplier of 1.04, but this drops to 0.91 by $Re = 130$. Comparing this image with those in figure 14 indicates that the wake undergoes a rapid transition to a two-layered wake close to the back of the cylinder. As this transition migrates upstream with increasing Reynolds number, the development of the mode A instability is suppressed. This is similar to the situation with the flat plate shown in figure 15(a), where mode A does not became unstable at all. Hence, at least in the near wake, there is a transition from a three-dimensional wake back to a two-dimensional wake. This ties in very well with the experimental result from figure 12, which shows that the Strouhal number curve beyond $Re = 120$ obtained from experiments (Radi *et al.* 2013) tracks the two-dimensional numerical prediction closely. Experimental flow visualisations also show that three-dimensionality in the near wake is suppressed at these Reynolds numbers, whilst the near wake is clearly three-dimensional at lower Reynolds numbers (Radi *et al.* 2013).

For $Ar = 0.25$, the wake remains two-dimensional beyond $Re = 125$ until another mode becomes unstable at $Re = 185$ (see table 3). The streamwise vorticity perturbation contours for that mode are shown in figure 17(b) and the spanwise contours in figure 17(c). The spatiotemporal symmetry is the same as mode A but the near wake and mode structure within the two-layered wake vortices are different. In particular, the spanwise vorticity contours show the characteristics of elliptic instability in these vortices, with a radial mode number of two, i.e. two radial nodes

Ar	First mode		Second mode	
	$Re_{c,QP}$	$\lambda_{c,QP}$	$Re_{c,AA}$	$\lambda_{c,AA}$
(Flat plate) 0.00	116	$5.0D$	141	$2.1D$
0.25	—	—	185	$1.3D$

TABLE 3. Critical Reynolds numbers and corresponding wavelengths for the initial quasi-periodic mode QP transition, and also mode AA transition, for small-aspect-ratio cylinders.

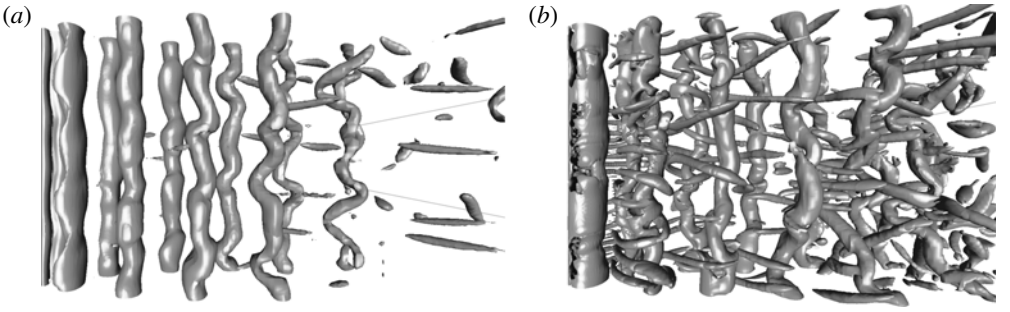

FIGURE 18. Wake vorticity structure for a flat plate, highlighted using the criterion of Jeong & Hussain (1995) with $\lambda_2 = -0.2$ from full three-dimensional simulations. Span shown is $16D$, using 128 Fourier planes: (*a*) $Re = 140$; (*b*) $Re = 180$.

in the perturbation field. (For mode A for $Ar = 0.25$ shown in figure 16, the radial mode number in the two-layer wake vortices is one.) This is consistent with the much shorter preferred wavelength of this new mode of $\lambda = 1.3D$ at onset. Interestingly, the equivalent mode is observed for the flat plate wake. This mode becomes unstable at $Re = 141$ (see table 3), and has a spanwise wavelength of $2.1D$. Note that this is a higher critical Reynolds number than reported previously (Thompson *et al.* 2006*b*), again because of the stronger influence of a shorter outflow length than expected, as discussed previously. The preferred wavelength at onset is considerably larger than that for the $Ar = 0.25$ cylinder of $1.3D$. However, this appears consistent with the larger size of the wake vortices for the flat plate, as can be seen in figure 17(*a*,*b*). For the flat plate, the quasi-periodic mode remains unstable for this Reynolds number, and remains so for higher Reynolds numbers. Hence, the flat plate wake does not return from a three-dimensional state to a two-dimensional state as the Reynolds number is increased.

Figure 18 shows isosurface visualisations from full three-dimensional simulations of the flat plate wake at $Re = 140$ (*a*) and $Re = 180$ (*b*). The isosurfaces correspond to $\lambda_2 = -0.2$ using the method of Jeong & Hussain (1995). It shows that increasing distortion of the spanwise vortical structures with increasing Reynolds number, and the increasing dominance of streamwise vortices. The transition to a saturated three-dimensional wake increases the Strouhal number considerably: for $Re = 140$, $St_{2D} \simeq 0.138$ and $St_{3D} \simeq 0.142$; and for $Re = 180$, $St_{2D} \simeq 0.136$ and $St_{3D} \simeq 0.151$. Again, this is consistent with the experimentally observed Strouhal number increase for a finite-thickness flat plate shown in figure 12.

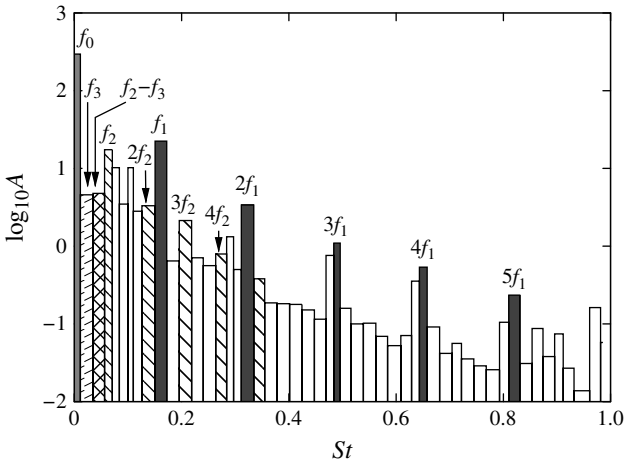

FIGURE 19. Frequency spectra from the DMD analysis for $Ar = 0.25$ and $Re = 150$. See the text for details.

3.10. *DMD of wakes*

Figures 3 and 4 show that these cylinder wakes can undergo various transitions as they advect downstream. For example, the wake for the $Ar = 0.25$ cylinder at $Re = 150$ shows the classical BvK wake very close to its base which rapidly undergoes transition to the two-layered wake within a few diameters. Further downstream, the two-layered wake becomes unstable and effectively sheds vortices forming a secondary vortex street at a lower frequency. That wake state develops a visible spatial oscillation, with a period approximately three times the second shedding frequency. Thus, there are at least three frequencies that dominate the wake over different spatial ranges. Note that the wake state shown in the image varies slowly over time, because the primary and secondary shedding frequency are not multiples, as is shown below. Of interest, the stability analysis of previous sections shows that the near wake is stable to three-dimensional perturbations in this Reynolds number range.

An analysis using DMD is warranted because of the different frequencies involved with the different spatial ranges of the wake. This was done using a sequence of 100 velocity fields separated by 0.5 time units to extract approximations to the Koopman modes, i.e. the Ritz vectors (Rowley *et al.* 2009; Schmid 2010, 2011). The frequency spectrum corresponding to the Ritz (eigen)values is shown in figure 19. The grey bar at zero frequency (f_0) corresponds to the mean mode. The black bars (f_1 ($St = 0.163$)) correspond to the near-wake shedding and its harmonics, the downward striped bars (f_2 ($St = 0.069$)) correspond to the secondary shedding mode and its harmonics, and the upward striped bar (f_3 ($St = 0.024$)) is associated with the meandering of the secondary wake towards the downstream end of the domain. In addition, the cross-hashed bar is associated with the frequency difference $f_2 - f_3$.

Reconstruction of the initial velocity field from the Ritz vectors is shown in figure 20. The top image shows spanwise vorticity for the first velocity field of the set. Figure 20(*b*) shows the zero-frequency (f_0) mode corresponding to the time mean vorticity field. Below this, figure 20(*c*) shows the DMD reconstruction just using the modes with frequency $f_0 + f_1 + 2f_1 + 3f_1 + 4f_1 + 5f_1$, i.e. the mean field together with the near-wake mode and its harmonics. This mode is localised in the

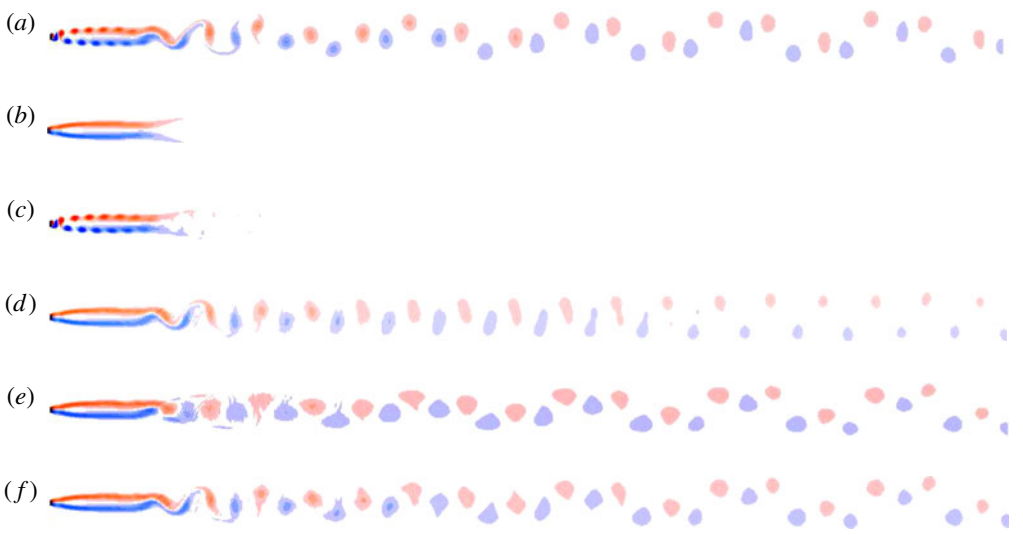

FIGURE 20. (Colour online) Reconstruction of wake for the $Ar = 0.25$ cylinder at $Re = 150$ from DMD modes. (*a*) Spanwise vorticity field for the original wake; (*b*) zero frequency DMD mode (f_0); (*c*) reconstruction of the near wake ($f_0 + f_1 + 2f_1 + 3f_1 + 4f_1 + 5f_1$); (*d*) reconstruction of secondary wake ($f_0 + f_2 + 2f_2 + 3f_2 + 4f_2 + 5f_2$); (*e*) low-order reconstruction of the meandering secondary wake ($f_1 + f_2 + f_3 + (f_2 - f_3)$); (*f*) higher-order reconstruction based on ($f_1 + f_2 + f_3 + (f_2 - f_3) + 2f_2 + 3f_2 + 4f_3 + 5f_2$). See the text for further details.

near wake, as expected, and duplicates the actual vorticity field there extremely well. The next image, figure 20(*d*), shows a reconstruction using modes corresponding to frequencies $f_0 + f_2$, which captures the secondary wake further downstream. This shows (near-)zero oscillation amplitude in the near wake, where the BvK and two-layered wakes reside. It persists further downstream, although weakened, to enable reconstruction of the meandering secondary wake state. The penultimate image corresponds to a reconstruction based on $f_0 + f_2 + f_3 + (f_2 - f_3)$, i.e. the mean field together with the secondary wake mode, the lower-frequency meandering mode and the difference between them. This reconstructs the meandering secondary wake towards the end of the domain particular well, although near the secondary transition the vortices are rather diffuse. The final image (figure 20*f*) is a reconstruction based on that combination together with the harmonics of the secondary wake mode ($f_0 + f_2 + f_3 + (f_2 - f_3) + 2f_2 + 3f_2 + 4f_2 + 5f_2$). This captures the wake downstream from the development of secondary shedding. From the vorticity field shown in figure 20(*a*), the secondary wake develops from merging of the upstream two-layer vortices while those latter vortices are still distinct, i.e. before those vortices have diffused to produce a locally time-independent wake. However, despite this, the ratio of the frequencies of the primary to secondary wake is not an integer, as it would be if the secondary wake vortices structures were obtained from direct merging of the primary two-layer vortices. This ratio is $St_1/St_2 = 0.163/0.069 = 2.36$. In addition, the ratio of the secondary wake frequency to the meandering frequency is $St_2/St_3 = 0.069/0.024 = 2.87$, again not an integer, but still close to 3 so that the meandering wavelength seems to be associated with groups of 3 vortices from the secondary wake. The upshot of this is that the wake snapshot shown in figure 20(*a*) is

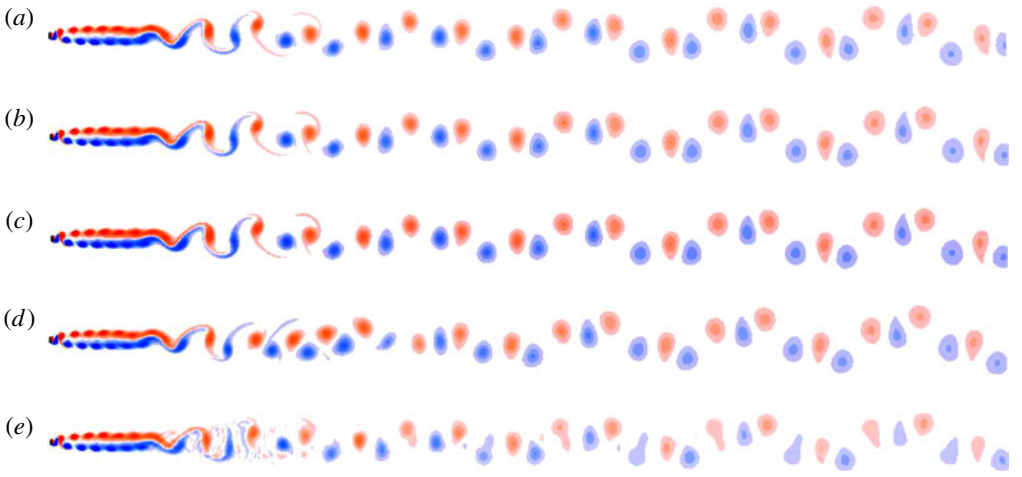

FIGURE 21. (Colour online) Development and reconstruction of wake for the $Ar = 0.25$ cylinder at $Re = 150$ at various times. (*a*) Spanwise vorticity field for the original wake ($t = 0$); (*b*) vorticity field approximately one meandering period later ($t = 43$); (*c*) DMD reconstruction at this time ($t = 43$) using all modes; (*d*) wake a further two meandering periods later ($t = 129$); (*e*) DMD reconstruction at that time ($t = 129$). The latter image shows that the near and far fields are reproduced reasonably accurately, but the intermediate wake is less accurate. See the text for further details.

not representative of all times, but changes slowly with time. For instance, figure 21 shows the wake at a number of different times. The first two images ((*a*) and (*b*)) show the wake approximately one meandering period apart. Indeed, these two wakes appear almost visually identical. The next image (*c*) shows that DMD reconstruction using all of the modes for the same time, which verifies that the reconstruction faithfully reproduces the actual velocity field. The next image (*d*) shows the wake at another two meandering periods later from direct simulations, which is well past the end time of the set of velocity fields used for the DMD analysis. This wake looks considerably different for the initial part of the secondary wake. Reconstruction of the wake through extrapolation up to this time using all of the DMD modes, i.e. extrapolating to non-dimensional time $t = 129$ with DMD analysis based on the time interval $t \leqslant 49.5$, is shown in the last image (*e*). This captures the near wake accurately and the far wake meandering reasonably well. It is less representative over the intermediate range downstream of where the secondary shedding starts.

It is interesting to see how many modes are required to capture the near-wake accurately. This is shown in figure 22. The top image shows the original vorticity field. The next five images shows a reconstruction using the mean mode and mode f_1 together with zero to four harmonics of f_1. Clearly most of the detail is accurately captured with just the first mode. Adding the next two harmonics improves the fidelity substantially, especially over the very near wake. The addition of four harmonics produces an image that is almost visually identical to the original, except for a very small amount of noise close to the forming vortex.

Finally, DMD is used to examine the differences in the wake structure between two- and three-dimensional simulations for the flat plate wake. The wake was examined at $Re = 140$ and 180 corresponding to the three-dimensional simulations of figure 18. In each case, 100 snapshots were used for the reconstruction spaced at 0.61 time

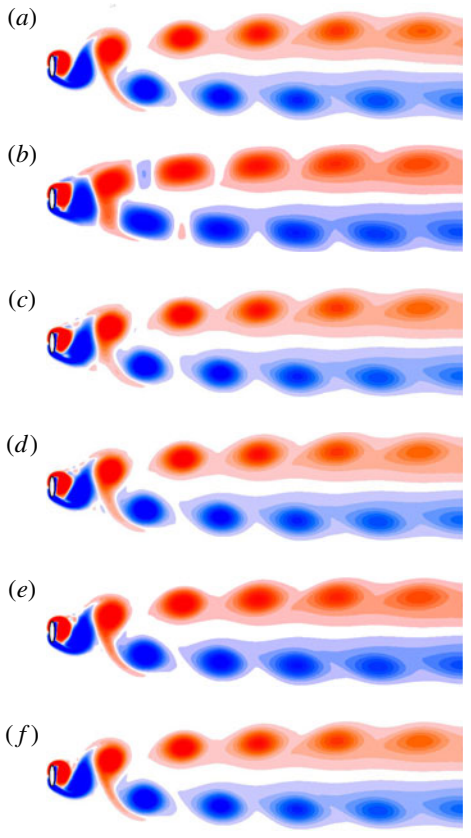

FIGURE 22. (Colour online) Reconstruction of the near wake using DMD modes. The top image shows the wake at zero time. The following images shows the near wake reconstruction based on the mean field together with mode f_1 and zero to four harmonics: (*a*) full field; (*b*) mode f_1; (*c*) modes $f_1 + 2f_1$; (*d*) modes $f_1 + 2f_1 + 3f_1$; (*e*) modes $f_1 + 2f_1 + 3f_1 + 4f_1$; (*f*) modes $f_1 + 2f_1 + 3f_1 + 4f_1 + 5f_1$.

units apart. The spanwise-averaged velocity was used for the analysis based on the three-dimensional simulations. Figure 23 shows the change to the mean centreline velocity determined from the mean DMD mode. At $Re = 140$, there is only a minor change to the near-wake centreline velocity variation between the two- and three-dimensional simulations. For the two-dimensional case, the velocity is close to zero up to $x/D \simeq 17$ downstream, while the three-dimensional result shows a velocity of considerably less than 10 % of the background velocity over the similar range. Further downstream, unsurprisingly, the two-dimensional velocity recovers towards the free-stream value considerably faster. The higher-Reynolds-number results are considerably different. The flow reversal is not observed in the three-dimensional case, and indeed the velocity recovery in the three-dimensional case is rapid. These observations are in accord with the DMD reconstructions shown at the right. They show the near-wake structure using the mean mode together with the DMD mode with the near-wake frequency and its first four harmonics. At the lower Reynolds number of $Re = 140$, even though transition occurs at $Re = 116$, the two- and three-dimensional solution-based reconstructions are very similar, indicating that the mean distortion of

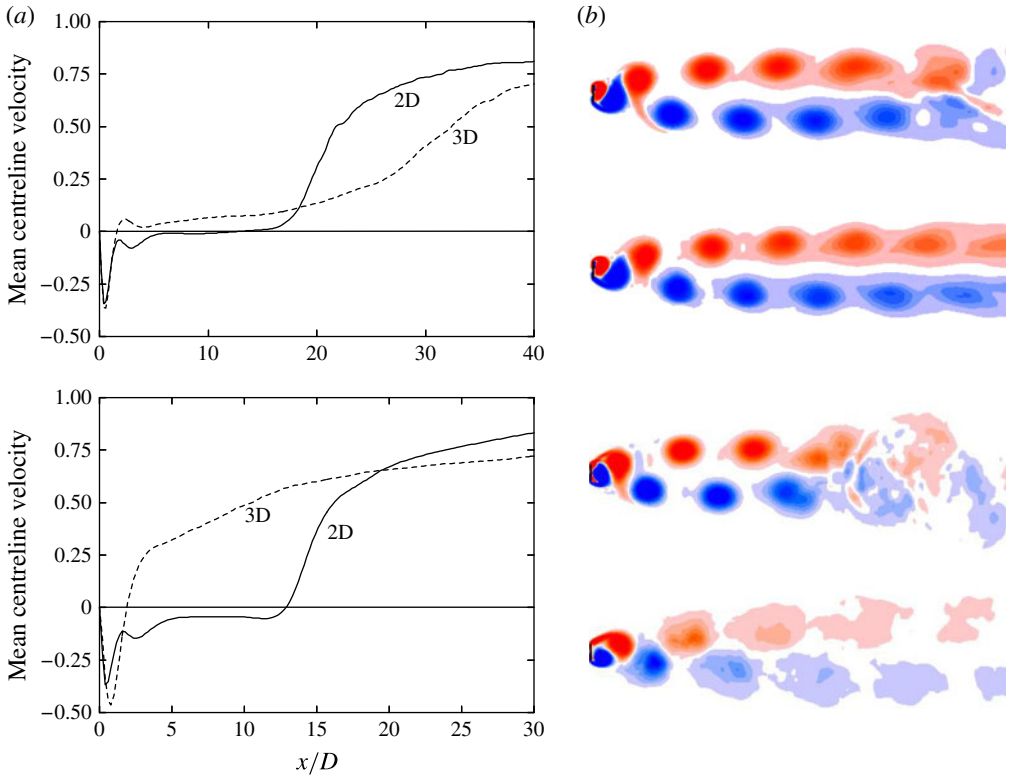

FIGURE 23. (Colour online) (*a*) Variation of the centreline velocity in the wake of a flat plate for $Re = 140$ (top) and $Re = 180$ (bottom). (*b*) Reconstruction of the near-wake vorticity field from DMD modes. The mean mode and the mode corresponding to the near-wake frequency, together with its first four harmonics, are used for the reconstruction. The top image of each set uses the two-dimensional fields and the lower one uses the three-dimensional simulation fields. Again, the upper and lower image sets correspond to $Re = 140$ and $Re = 180$, respectively.

the two-dimensional vortex rollers is little affected by the three-dimensionality of the wake. This is not true at the higher Reynolds number of $Re = 180$, where is it clear that the three-dimensional reconstruction shows diffuse near-wake vortices relative to the compact two-dimensional wake vortices. This is consistent with the stronger induced roller distortion in the near wake at the higher Reynolds number.

3.11. *Fourier analysis of centreline velocity*

The dominant wake frequencies were further analysed using standard Fourier analysis of the cross-stream velocity along the wake centreline. For the same case as examined above for the DMD analysis, i.e. $Ar = 0.25$, $Re = 150$, figure 24(*a*) shows the spectral power of the cross-stream velocity component at various downstream distances. This is summarised in figure 24(*b*) which shows the dominant frequency components as a function of downstream distance. The velocity was sampled at $\Delta t = 0.01$ time units to produce $N = 2^{17} = 131\,072$ measurements. This set was then processed using a fast Fourier transform (FFT) to produce these plots. This gives a frequency resolution of $\Delta St = 2/(N\Delta t) = 0.0015$, with the data set consisting of more than 200 near-wake

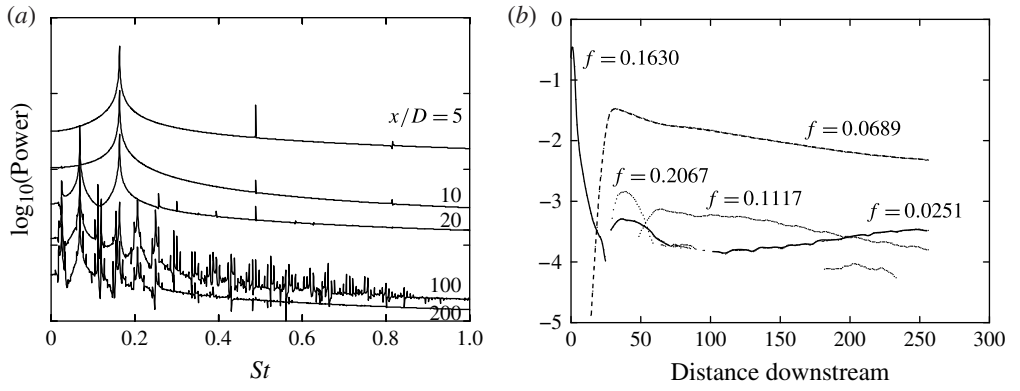

FIGURE 24. Spectral analysis of wake for the $Ar = 0.25$ cylinder at $Re = 150$. (*a*) Power spectra at different downstream distances. (*b*) Power of the dominant frequency components as a function of downstream distance.

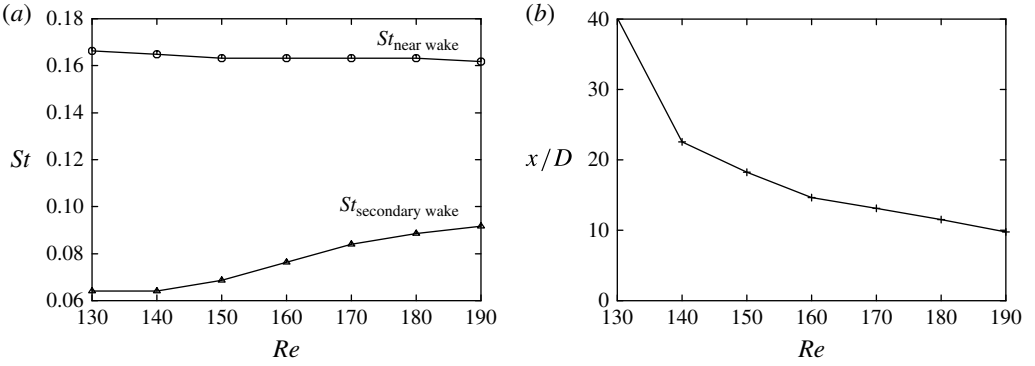

FIGURE 25. (*a*) Near-wake and secondary-wake frequencies as a function of Reynolds number for the $Ar = 0.25$ cylinder. (*b*) Downstream position at which the wake undergoes transition from the near wake to the secondary wake.

shedding cycles. The principal peaks corresponding to the near-wake, secondary wake and meandering frequencies ($St_1 = 0.1630$, $St_2 = 0.0689$, $St_3 = 0.0251$) match those found from the 100 sample DMD analysis (0.1626, 0.0689, 0.0243, respectively) to within the frequency resolution of the Fourier analysis. The transition from the near wake to the secondary wake is further quantified in figure 25. The left-hand figure shows the variation of the near- and secondary-wake frequencies as a function of Reynolds number. For lower Reynolds number, the secondary frequency is less than half of the near-wake frequency. The ratio is close to 2 for $Re \simeq 170$. Thus, again, it is clear that the secondary wake does not result from direct merging of a discrete number of near-wake vortices. At higher Reynolds numbers, for example $Re = 160$, the secondary wake vortices merge further downstream resulting in a lowering of the dominant wake frequency from $St = 0.0733$ to $St = 0.0565$. This occurs a long way downstream at $x/D \simeq 250$. The transition from the near wake to the secondary wake occurs progressively closer to the cylinder. It is quantified in figure 25 as the position where the spectral power corresponding to the near- and secondary-wake frequencies are equal.

4. Conclusions

The critical Reynolds numbers and Strouhal frequencies for the initial transition to unsteady periodic flow have been accurately determined for elliptical cylinders of different aspect ratios. These results correlate well with previous studies when the effects of blockage of previous studies are taken into account. The two-dimensional simulations spanned Reynolds numbers up to 200, corresponding to the upper limit of two-dimensional shedding for the circular cylinder. This produces a rich variety of wake states. As the aspect ratio is lowered and the Reynolds number is increased, the wake undergoes a series of changes that are not normally seen with the circular cylinder wake. In the most extreme cases, the near-wake BvK shedding rapidly shifts to a two-layered structure within a few diameters downstream. Further downstream, the two-layered wake can become unstable, with an oscillation developing and a secondary aligned vortex street the result. This may form either downstream of where the two-layered vortices diffuse and merge due to a hydrodynamic instability (Durgin & Karlsson 1971) to reach a time-independent state, or prior to this, when the two-layered vortices are still discrete. In either case, the near-wake and secondary-wake frequencies are not commensurate so that the secondary-wake vortices are not the result of merging of a discrete number of two-layer vortices. The secondary wake initially takes the form of a typical BvK vortex street, but as the Reynolds number is increased, that street develops (near-)periodic oscillations and even chaotic behaviour with further merging of vortices, the formation of identifiable vortex pairs and substantial increases in the wake width. It is clear that decreasing the aspect ratio results in a substantial increase in the circulation feeding into the wake, due to the increased speed up of the flow as it passes around the top of the cylinder. For a flat plate, this circulation is approximately a factor of two greater than for a circular cylinder at $Re = 200$, hence the wake vortices are stronger and also larger.

The centreline wake deficit variation with Reynolds number has also been quantified. The downstream variation is surprisingly different from that of a circular cylinder once the two-layer wake develops. This leads to a very low mean velocity due to the combined influence of the offset negative and positive lines of vortices. Even for the $Ar = 0.5$ cylinder, the mean centreline velocity is close to zero downstream to approximately 20 diameters. For the flat plate at $Re = 150$ and above, there is a significant reverse flow further downstream from the immediate near wake (as was observed by Saha (2013)).

The Strouhal/Reynolds number variations from the two-dimensional simulations are quantified. These show a considerably more complex behaviour than that for a circular cylinder. The agreement with experimental results is favourable, when the flow is not three-dimensional. The onset of three-dimensional flow is also predicted. In this case, decreasing the aspect ratio decreases the Reynolds number at which the BvK near wake undergoes downstream transition to the two-layered wake. This strongly affects the transition scenario. For aspect ratios of 0.5 and above, the initial transition is equivalent to the mode A transition for a circular cylinder, even though the critical Reynolds number decreases substantially as the aspect ratio decreases. At $Ar = 0.25$, the initial transition is also similar to mode A. The critical Reynolds number is approximately 88. However, increasing the Reynolds number leads to such a change in the two-dimensional wake structure that mode A is no longer unstable beyond $Re \simeq 125$. Thus, at least the near-wake returns to a two-dimensional state. This two-dimensional state remains stable until $Re = 185$, when another three-dimensional mode with the same spatiotemporal symmetry as mode A but a much shorter wavelength ($\lambda = 1.3D$) becomes unstable. However,

the wake shows little resemblance to a classical BvK vortex street at this Reynolds number. For the flat plate, the transition to the two-layered wake state occurs at an even lower Reynolds number. This seems to prevent mode A becoming unstable at all. Instead, at $Re = 116$, a quasi-periodic three-dimensional mode becomes unstable, and at $Re = 141$ another mode which has the same period as the base flow also becomes unstable. This second mode appears to be equivalent to the mode causing the second three-dimensional transition for the $Ar = 0.25$ cylinder. Three-dimensional simulations at $Re = 140$ and $Re = 180$ confirm the three-dimensional nature of the wake at these Reynolds numbers and show that the major distortion of the two-dimensional vortex rollers occurs towards the end of the two-layered wake region. The three-dimensional wake has a higher Strouhal number than its two-dimensional counterpart.

DMD was also applied to the $Ar = 0.25$ wake at $Re = 150$. This case corresponds to when the wake shows quite distinct temporal behaviours over different spatial ranges. The analysis using only a short time sequence of 100 snapshots was able to extract the spatially localised wake components together with accurate determination of their corresponding frequencies. Those frequencies agree with the dominant frequencies obtained from Fourier analysis of the cross-stream velocity on the centreline using much longer and finer temporal data sets. The DMD analysis allows an accurate reconstruction of the wake state at any time using just the dominant modes and their harmonics.

Acknowledgements

The authors acknowledge computing-time support from the Victorian Life Sciences Computation Initiative (VLSCI) and the National Computational Infrastructure (NCI). The authors acknowledge financial support from Australian Research Council Discovery Project grants DP110102141 and DP130100822.

REFERENCES

ALBAREDE, P. & MONKEWITZ, P. A. 1992 A model for the formation of oblique shedding and Chevron patterns in cylinder wakes. *Phys. Fluids* A **4** (4), 744–756.

ALEKSYUK, A. I., SHKADOVA, V. P. & SHKADOV, V. Y. 2012 Formation, evolution, and decay of a vortex street in the wake of a streamlined body. *Moscow Univ. Mech. Bull.* **67** (3), 53–61.

BARKLEY, D. & HENDERSON, R. D. 1996 Three-dimensional Floquet stability analysis of the wake of a circular cylinder. *J. Fluid Mech.* **322**, 215–241.

BEHARA, S. & MITTAL, S. 2010 Wake transition in flow past a circular cylinder. *Phys. Fluids* **22** (11), 114104.

BÉNARD, H. 1908 Formation de centres de giration à l'àrriere d'un obstacle en mouvement. *C. R. Acad. Sci. Paris* **147**, 839–842.

CHAURASIA, H. K. & THOMPSON, M. C. 2012 Three-dimensional instabilities in the boundary-layer flow over a long rectangular plate. *J. Fluid Mech.* **681**, 411–433.

CHORIN, A. J. 1968 Numerical solution of the Navier–Stokes equations. *Maths Comput.* **22**, 745–762.

CIMBALA, J. M. 1984 Large structure in the far wakes of two-dimensional bluff bodies. PhD thesis, Graduate Research Laboratories.

CIMBALA, J. M., NAGIB, H. M. & ROSHKO, A. 1988 Large structure in the far wakes of two-dimensional bluff bodies. *J. Fluid Mech.* **190**, 265–298.

DURGIN, W. W. & KARLSSON, S. K. F. 1971 On the phenomenon of vortex street breakdown. *J. Fluid Mech.* **48** (03), 507–527.

DUSEK, J., LE GAL, P. & FRAUNIE, D. P. 1994 A numerical and theoretical study of the first Hopf bifurcation in a cylinder wake. *J. Fluid Mech.* **264**, 59–80.

EISENLOHR, H. & ECKELMANN, H. 1989 Vortex splitting and its consequences in the vortex street wake of cylinders at low Reynolds number. *Phys. Fluids* A **1** (2), 189–192.

FAGE, A. & JOHANSEN, F. C. 1927 On the flow of air behind an inclined flat plate of infinite span. *Proc. R. Soc. Lond.* A **116** (773), 170–197.

GRIFFITH, M. D., LEWEKE, T., THOMPSON, M. C. & HOURIGAN, K. 2008 Steady inlet flow in stenotic geometries: convective and absolute instabilities. *J. Fluid Mech.* **616**, 111–133.

GRIFFITH, M. D., LEWEKE, T., THOMPSON, M. C. & HOURIGAN, K. 2010 Convective instability in steady stenotic flow: optimal transient growth and experimental observation. *J. Fluid Mech.* **655**, 504–514.

HENDERSON, R. D. 1995 Details of the drag curve near the onset of vortex shedding. *Phys. Fluids* **7** (9), 2102–2104.

HENDERSON, R. D. 1997 Nonlinear dynamics and pattern formation in turbulent wake transition. *J. Fluid Mech.* **352** (1), 65–112.

JACKSON, C. P. 1987 A finite-element study of the onset of vortex shedding in flow past variously shaped bodies. *J. Fluid Mech.* **182**, 23–45.

JEONG, J. & HUSSAIN, F. 1995 On the identification of a vortex. *J. Fluid Mech.* **285**, 69–94.

JOHNSON, S. A., THOMPSON, M. C. & HOURIGAN, K. 2004 Predicted low frequency structures in the wake of elliptical cylinders. *Eur. J. Mech. (*B*/Fluids)* **23** (1), 229–239.

KARASUDANI, T. & FUNAKOSHI, M. 1994 Evolution of a vortex street in the far wake of a cylinder. *Fluid Dyn. Res.* **14** (6), 331–352.

KÁRMÁN, TH. V. 1911 Über den Mechanismus des Widerstandes, den ein bewegter Körper in einer Flüsseigkeit erfährt. *Gött. Nachr.* 509–511.

KARNIADAKIS, G. E., ISRAELI, M. & ORSZAG, S. A. 1991 High-order splitting methods for the incompressible Navier–Stokes equations. *J. Comput. Phys.* **97**, 414–443.

KARNIADAKIS, G. E. & SHERWIN, S. J. 2005 *Spectral/HP Methods for Computational Fluid Dynamics*. Oxford University Press.

KARNIADAKIS, G. E. & TRIANTAFYLLOU, G. S. 1992 Three-dimensional dynamics and transition to turbulence in the wake of bluff objects. *J. Fluid Mech.* **238**, 1–30.

KUMAR, B. & MITTAL, S. 2006 Effect of blockage on critical parameters for flow past a circular cylinder. *Intl J. Numer. Meth. Fluids* **50** (8), 987–1001.

KUMAR, B. & MITTAL, S. 2012 On the origin of the secondary vortex street. *J. Fluid Mech.* **711**, 641–666.

LE GAL, P., NADIM, A. & THOMPSON, M. C. 2001 Hysteresis in the forced Stuart–Landau equation: application to vortex shedding from an oscillating cylinder. *J. Fluids Struct.* **15**, 445–457.

LEONTINI, J. S., LO JACONO, D. & THOMPSON, M. C. 2013 Wake states and frequency selection of a streamwise oscillating cylinder. *J. Fluid Mech.* **730**, 162–192.

LEONTINI, J. S., THOMPSON, M. C. & HOURIGAN, K. 2007 Three-dimensional transition in the wake of a transversely oscillating cylinder. *J. Fluid Mech.* **577**, 79–104.

MAMUN, C. K. & TUCKERMAN, L. S. 1995 Asymmetry and Hopf-bifurcation in spherical Couette flow. *Phys. Fluids* **7**, 80–91.

MILLER, G. D. & WILLIAMSON, C. H. K. 1994 Control of three-dimensional phase dynamics in a cylinder wake. *Exp. Fluids* **18** (1), 26–35.

MODI, V. J. & DIKSHIT, A. K. 1975 Near-wakes of elliptic cylinders in subcritical flow. *AIAA J.* **13** (4), 490–497.

MODI, V. J. & WILAND, E. 1970 Unsteady aerodynamics of stationary elliptic cylinders in subcritical flow. *AIAA J.* **8** (10), 1814–1821.

MONKEWITZ, P. A. 1988 The absolute and convective nature of instability in two-dimensional wakes at low Reynolds numbers. *Phys. Fluids* **31** (5), 999–1006.

NAJJAR, F. M. & BALACHANDAR, S. 1998 Low-frequency unsteadiness in the wake of a normal flat plate. *J. Fluid Mech.* **370**, 101–147.

NORBERG, C. 1987 Effects of Reynolds number and a low-intensity free stream turbulence on the flow around a circular cylinder. PhD thesis, Chalmers University of Technology.

OTA, T., NISHIYAMA, H. & TAOKA, Y. 1987 Flow around an elliptic cylinder in the critical Reynolds number regime. *Trans. ASME J. Fluids Engng* **109** (2), 149–155.

RADI, A., THOMPSON, M. C., SHERIDAN, J. & HOURIGAN, K. 2013 From the circular cylinder to the flat plate wake: the variation of Strouhal number with Reynolds number for elliptical cylinders. *Phys. Fluids* **25**, 101706.

RAO, A., LEONTINI, J. S., THOMPSON, M. C. & HOURIGAN, K. 2013*a* Three-dimensionality in the wake of a rotating cylinder in a uniform flow. *J. Fluid Mech.* **717**, 1–29.

RAO, A., THOMPSON, M. C., LEWEKE, T. & HOURIGAN, K. 2013*b* Dynamics and stability of the wake behind tandem cylinders sliding along a wall. *J. Fluid Mech.* **722**, 291–316.

ROSHKO, A. 1954 *On the Drag and Shedding Frequency of Two-Dimensional Bluff Bodies*. National Aeronautics and Space Administration.

ROWLEY, C. W., MEZIĆ, I., BAGHERI, S., SCHLATTER, P. & HENNINGSON, D. S. 2009 Spectral analysis of nonlinear flows. *J. Fluid Mech.* **641**, 115–127.

RYAN, K., THOMPSON, M. C. & HOURIGAN, K. 2005 Three-dimensional transition in the wake of elongated bluff bodies. *J. Fluid Mech.* **538**, 1–29.

SAHA, A. K. 2007 Far-wake characteristics of two-dimensional flow past a normal flat plate. *Phys. Fluids* **19**, 128110.

SAHA, A. K. 2013 Direct numerical simulation of two-dimensional flow past a normal flat plate. *J. Engng Mech. ASCE* **12**, 1894–1901.

SCHMID, P. J. 2010 Dynamic mode decomposition of numerical and experimental data. *J. Fluid Mech.* **656**, 5–28.

SCHMID, P. J. 2011 Application of the dynamic mode decomposition to experimental data. *Exp. Fluids* **50**, 1123–1130.

SHINTANI, K., UMEMURA, A. & TAKANO, A. 1983 Low-Reynolds-number flow past an elliptic cylinder. *J. Fluid Mech.* **136** (1), 277–289.

STEWART, B. E., THOMPSON, M. C., LEWEKE, T. & HOURIGAN, K. 2010 The wake behind a cylinder rolling on a wall at varying rotation rates. *J. Fluid Mech.* **648**, 225–256.

STROUHAL, V. 1878 Üeber eine besondere Art der Tonerregung. *Ann. Phys.* **241** (10), 216–251.

STRYKOWSKI, P. J. & SREENIVASAN, K. R. 1990 On the formation and suppression of vortex 'shedding' at low Reynolds numbers. *J. Fluid Mech.* **218**, 71–107.

TANEDA, S. 1959 Downstream development of the wakes behind cylinders. *J. Phys. Soc. Japan* **14** (6), 843–848.

THOMPSON, M. C., HOURIGAN, K., CHEUNG, A. & LEWEKE, T. 2006*a* Hydrodynamics of a particle impact on a wall. *Appl. Math. Model.* **30**, 1356–1369.

THOMPSON, M. C., HOURIGAN, K., RYAN, K. & SHEARD, G. J. 2006*b* Wake transition of two-dimensional cylinders and axisymmetric bluff bodies. *J. Fluids Struct.* **22** (6–7), 793–806.

THOMPSON, M. C., HOURIGAN, K. & SHERIDAN, J. 1996 Three-dimensional instabilities in the wake of a circular cylinder. *Exp. Therm. Fluid Sci.* **12** (2), 190–196.

THOMPSON, M. C., LEWEKE, T. & HOURIGAN, K. 2007 Sphere-wall collisions: vortex dynamics and stability. *J. Fluid Mech.* **575**, 121–148.

THOMPSON, M. C., LEWEKE, T. & WILLIAMSON, C. H. K. 2001 The physical mechanism of transition in bluff body wakes. *J. Fluids Struct.* **15** (3–4), 607–616.

TSUBOI, K. & OSHIMA, Y. 1985 Merging of two-dimensional vortices by the discrete vortex method. *J. Phys. Soc. Japan* **54** (6), 2137–2145.

VOROBIEFF, P., GEORGIEV, D. & INGBER, M. S. 2002 Onset of the second wake: dependence on the Reynolds number. *Phys. Fluids* **14** (7), L53–L56.

WILLIAMSON, C. H. K. 1988 The existence of two stages in the transition to three-dimensionality of a cylinder wake. *Phys. Fluids* **31** (11), 3165–3168.

WILLIAMSON, C. H. K. 1989 Oblique and parallel modes of vortex shedding in the wake of a circular cylinder at low Reynolds numbers. *J. Fluid Mech.* **206**, 579–627.

WILLIAMSON, C. H. K. 1996*a* Three-dimensional wake transition. *J. Fluid Mech.* **328**, 345–407.

WILLIAMSON, C. H. K. 1996*b* Vortex dynamics in the cylinder wake. *Annu. Rev. Fluid Mech.* **28** (1), 477–539.

WILLIAMSON, C. H. K. & PRASAD, A. 1993 A new mechanism for oblique wave resonance in the far wake. *J. Fluid Mech.* **256**, 269–313.

YANG, D., NARASIMHAMURTHY, V. D., PETTERSEN, B. & ANDERSSON, H. I. 2012 Three-dimensional wake transition behind an inclined flat plate. *Phys. Fluids* **24** (9), 094107.

ZHANG, H.-Q., FEY, U., NOACK, B. R., KONIG, M. & ECKELMANN, H. 1995 On the transition of the cylinder wake. *Phys. Fluids* **7** (4), 779–794.